




2016

New Methods To Assess Protein Folding And Conformational Dynamics

Chun-Wei Lin

University of Pennsylvania, linchun@sas.upenn.edu

Follow this and additional works at: <https://repository.upenn.edu/edissertations>

 Part of the [Biophysics Commons](#), and the [Physical Chemistry Commons](#)

Recommended Citation

Lin, Chun-Wei, "New Methods To Assess Protein Folding And Conformational Dynamics" (2016). *Publicly Accessible Penn Dissertations*. 2425.

<https://repository.upenn.edu/edissertations/2425>

This paper is posted at ScholarlyCommons. <https://repository.upenn.edu/edissertations/2425>

For more information, please contact repository@pobox.upenn.edu.

New Methods To Assess Protein Folding And Conformational Dynamics

Abstract

A protein's folding and conformational energy landscape depends on a large number of molecular degrees of freedom and interactions. As a result, different proteins can follow different sequences of events moving toward the native state along the course of folding. For example, the underlying structural organization and ordering can occur locally first and then globally, or vice versa. In addition, the associated conformational transitions can take place over a wide range of timescales. Because of these complexities, arriving at a detailed assessment and understanding of the folding dynamics and mechanism of any protein via a single type of experiment is challenging, and sometimes impossible. As such, over the past two decades, many different experimental methods have been employed to study how proteins fold among which, the laser-induced temperature-jump (T-jump) technique has emerged as a powerful tool to measure protein folding kinetics occurring on the nanosecond and microsecond timescales. Herein, we further expand the utility of the T-jump technique. First, we introduce a new form of the T-jump technique (referred to as VIPT-jump) that can be used to distinguish between different folding mechanisms. Second, we apply the VIPT-jump concept to better understand the folding dynamics of an alanine-based α -helix, and, in conjunction with theoretical modeling, we are able to determine the long-sought microscopic rate constants of the helical nucleation and propagation processes. Third, we develop a new method to extend the time window of observation in a T-jump experiment to the millisecond timescale. In a parallel effort, we demonstrate that quenching the fluorescence of a dye molecule by a tryptophan residue via photoinduced electron transfer mechanism can be used to interrogate the conformational dynamics of proteins that are crucial for function. Applying this method to the M2 proton channel of the Influenza A virus allow us to determine, for the first time, the gating dynamics of the tryptophan tetrad in this membrane protein.

Degree Type

Dissertation

Degree Name

Doctor of Philosophy (PhD)

Graduate Group

Chemistry

First Advisor

Gai Feng

Keywords

helix nucleation and propagation, M2 proton channel, one-state (downhill) folding, protein folding, reverse micelle, VIPT jump

Subject Categories

Biophysics | Chemistry | Physical Chemistry

NEW METHODS TO ASSESS PROTEIN FOLDING AND CONFORMATIONAL DYNAMICS

Chun-Wei Lin

A DISSERTATION

in

Chemistry

Presented to the Faculties of the University of Pennsylvania

in

Partial Fulfillment of the Requirements for the

Degree of Doctor of Philosophy

2016

Supervisor of Dissertation

Dr. Feng Gai

Edmund J. and Louise W. Kahn Endowed Term Professor of Chemistry

Graduate Group Chairperson

Dr. Gary A. Molander

Hirschmann-Makineni Professor of Chemistry

Dissertation Committee

Dr. Masha I. Lester, (Chair), Edmund J. Kahn Distinguished Professor

Dr. Tobias Baumgart, Professor of Chemistry

Dr. Zahra Fakhraai, Professor of Chemistry

ACKNOWLEDGEMENTS

At first, I would like to thank my advisor, Feng Gai. For these six years, I have learned so much from him and benefited a lot from his guide. Without him, everything in this thesis becomes almost impossible and could not even exist. I really appreciate the challenging projects which he gave to me and the way that he encouraged me to leave my comforter zone to explore the science. At the beginning of being a Ph. D. student, I tended to claim myself as an experimentalist. Especially for the theoretical simulations which involve much of computer coding, I always try to stay away since I had a hard time with computer coding when I was an undergraduate student. However, Dr. Gai convinced me that I should push my scientific frontier further into the interface between the experiment and the theory which actually requires not only the experimental skills, but also much modeling and fitting along with program coding. The challenge is high and I encountered so much frustration during the time. However, I finally realize that I actually learn so much more than any other period in my life. I would still make the same decision if time could go back and I could decide the path of my Ph. D. again. Without my advisor, I would not even give it a try. Thank you, Dr. Gai. Here I would also like to thank my committee members, Professors Marsha Lester, Tobias Baumgart, and Zahra Fakhraai for their effort of keeping me on the track of finishing my projects. Their advices from our meetings are very helpful.

Second, I want to thank my former and current labmates, Dr. Lin Guo, Dr. Arnaldo Serrano, Dr. Kate Smith-Dupont, Dr. Ileana Pazos, Dr. Beatrice Markiewicz, Dr. Tom Troxler, Dr. Jian-Xin Chen, Dr. Bei Ding, Rachel Abaskharon, Mary Rose Hilaire,

Ismail Ahmed, Jeff Rodgers, Debopreeti Mukherjee, Arusha Acharyya, Dr. Wenkai Zhang, Dr. Natalia Rubtsova, Dr. Kwang-Im Oh, Dr. Thomas Measey, Dr. Matthias Waegle. I would like to especially emphasize my gratitude to Dr. Rob Culik who not only teaches me how to do the experiments, but also becomes my mentor to answer all kind of my questions. To have you as my labmate as well as my friend is really my pleasure.

Third, I want to thank my friends and classmates, Yi-Ju Chen, Dr. Zheng Shi, Dr. Fan Zheng, Chun Liu, Dr. Zhengzheng Liao, Dr. Sheng-Chun Sha, Dr. Tingting Wu, Dr. Shi Liu, Dr. Diomedes Saldana Greco, Dr. Xinle Liu, Dr. Fang Liu, Dr. Qingjie Luo, Dr. Xiaojing Liu, Dr. Zhiming Chen, Yu-Fun Hsieh, Yi-Chih Lin, and Hao Chou, for making my life here full of fun. I want to emphasize my thank to Dr. Chih-Jung Hsu, Dr. Chi-Mon Chen, Dr. Wan-Ting Hsieh and Dr. Yu-Hsiu Wang for sharing your life and researching experience here with me especially when I just newly came to the united states six year ago. Furthermore, I want to thank Dr. Chin-Kuei Kuo for spending so much time and even coming back twice after his graduation to teach me how to do PAINT experiment.

Finally and most important of all, I want to thank my family especially my parents. I feel sorry that I was not around with you for these years. If you do feel anything that you are proud of about me, you actually own the most credit of them because I would not even come any close to this step without the support from you. Mom and dad, I love you.

ABSTRACT

NEW METHODS TO ASSESS PROTEIN FOLDING AND CONFORMATIONAL DYNAMICS

Chun-Wei Lin

Feng Gai

A protein's folding and conformational energy landscape depends on a large number of molecular degrees of freedom and interactions. As a result, different proteins can follow different sequences of events moving toward the native state along the course of folding. For example, the underlying structural organization and ordering can occur locally first and then globally, or vice versa. In addition, the associated conformational transitions can take place over a wide range of timescales. Because of these complexities, arriving at a detailed assessment and understanding of the folding dynamics and mechanism of any protein via a single type of experiment is challenging, and sometimes impossible. As such, over the past two decades, many different experimental methods have been employed to study how proteins fold among which, the laser-induced temperature-jump (*T*-jump) technique has emerged as a powerful tool to measure protein folding kinetics occurring on the nanosecond and microsecond timescales. Herein, we further expand the

utility of the *T*-jump technique. First, we introduce a new form of the *T*-jump technique (referred to as VIPT-jump) that can be used to distinguish between different folding mechanisms. Second, we apply the VIPT-jump concept to better understand the folding dynamics of an alanine-based α -helix, and, in conjunction with theoretical modeling, we are able to determine the long-sought microscopic rate constants of the helical nucleation and propagation processes. Third, we develop a new method to extend the time window of observation in a *T*-jump experiment to the millisecond timescale. In a parallel effort, we demonstrate that quenching the fluorescence of a dye molecule by a tryptophan residue via photoinduced electron transfer mechanism can be used to interrogate the conformational dynamics of proteins that are crucial for function. Applying this method to the M2 proton channel of the Influenza A virus allow us to determine, for the first time, the gating dynamics of the tryptophan tetrad in this membrane protein.

TABLE OF CONTENTS

1. Introduction.....	1
2. Methods.....	7
2.1 Circular Dichroism (CD) Spectroscopy.....	8
2.2 Fourier-Transform Infrared (FTIR) Spectroscopy and IR Spectroscopy of Proteins	8
2.3 Laser-Induced Temperature-jump (<i>T</i> -jump) Spectroscopy	10
2.2 Fluorescence Correlation Spectroscopy (FCS).....	11
3. Using VIPT-Jump to Distinguish Between Different Folding	13
Mechanisms: Application to BBL and a Trpzip	13
3.1 Abstract.....	14
3.2 Introduction.....	15
3.3 Results and Discussion	17
3.4 Conclusion	25
3.5 Experimental Section.....	27
4. Extracting the α -Helix Nucleation and Propagation Rates from the VIPT-Jump Kinetics of an Alanine-Based Peptide.....	50
4.1 Abstract.....	51
4.2 Introduction.....	52
4.3 Results and Discussion	55
4.4 Conclusion	65

4.5 Computational Methods.....	66
5. Measuring <i>T</i> -Jump Kinetics from Nanometer-Sized Water Droplets in Reverse Micelles.....	77
5.1 Abstract.....	78
5.2 Introduction.....	79
5.3 Results and Discussion	82
5.4 Conclusion	87
5.5 Experimental Section.....	88
6. Conformational Dynamics of Influenza A M2 Proton Channel Probed by Photoinduced Electron Transfer Fluorescence-Quenching Correlation Spectroscopy.....	99
6.1 Abstract.....	100
6.2 Introduction.....	101
6.3 Results and Discussion	104
6.4 Conclusion	107
6.5 Experimental Section.....	108
7. Future Direction	118
8. References.....	121

LIST OF FIGURES

Figure 3.1. Cartoon depiction of representative folding free energy surfaces. (A) two-state folding scenario, (B) and (C) three-state folding scenarios with the observable intermediate state located on either side of the major folding barrier, and (D) downhill or one-state folding scenario.	29
Figure 3.2. Relative free energies of U, I, and F in a three-state folding scenario at 298.0 (red), 310.5 (orange), and 323.0 K (blue), respectively, with the intermediate state located at either the left- (A) or right-hand (B) side of the major folding free energy barrier.....	30
Figure 3.3. Simulated relaxation kinetics in response to T -jumps from different initial temperatures to the same final temperature, as indicated, obtained via LD simulations using the free energy surfaces shown in the inset.....	31
Figure 3.4. Comparison of the normalized conformational relaxation kinetics of BBL obtained with a probing frequency of 1668 cm^{-1} and at a final temperature of $46.8\text{ }^{\circ}\text{C}$, from two different initial temperatures, as indicated. The red lines are fits of the data to a single-exponential function, and the resulting time constants are reported in Table 3.4..	32
Figure 3.5. Comparison of the normalized conformational relaxation kinetics of BBL obtained with a probing frequency of 1668 cm^{-1} and at a final temperature of $57.0\text{ }^{\circ}\text{C}$, from two different initial temperatures, as indicated. The red lines are fits of the data to a single-exponential function and the resulting time constants are reported in Table 3.4...	33
Figure 3.6. Comparison of the normalized conformational relaxation kinetics of Trpzip-2c obtained at a final temperature of $61.8\text{ }^{\circ}\text{C}$, from different initial temperatures, as indicated. The probing frequency was 1630 cm^{-1}	34

Figure 3.7. LD fits (red) of the experimental IR relaxation kinetics of BBL from Figure 3.4, using the free energy surfaces shown in the inset. The resulting effective conformational diffusion coefficients are given in the text.	35
Figure 3.7. Far-UV CD spectrum of BBL, collected at 1°C.....	36
Figure 3.9. Relative population changes in response to a <i>T</i> -jump of 298 to 323 K (red) or 310.5 to 323 K (blue), for the two three-state folding mechanisms (A or B, as indicated) presented in Figure 3.2.....	37
Figure 3.10. Overlay of CD thermal melting curve of BBL (blue) with IR melting curve probed at 1668 cm ⁻¹ (red).....	38
Figure 3.11. Single exponential fits of the Langevin Dynamics signal traces in Figure 3.3, with temperature jumps as indicated.....	39
Figure 3.12. Difference FTIR spectra of BBL in the amide I' region, generated by subtracting the FTIR spectrum at 6.9 °C from those measured at higher temperatures (the highest temperature was 62.9 °C).	40
Figure 3.13. Conformational relaxation kinetics of BBL obtained with a probing frequency of 1668 cm ⁻¹ after a <i>T</i> -jump from 49.2 to 50.7 °C.	41
Figure 3.14. Simulated relaxation kinetics in response to <i>T</i> -jumps from different initial temperatures to the same final temperature, as indicated, for an incipient downhill folding scenario.	42
Figure 3.15. Free energy surfaces for an incipient downhill folding scenario used to simulate relaxation kinetics in Figure 3.14.	43
Figure 3.16. Relaxation kinetics of Trpzip-2c with different magnitude <i>T</i> -jumps, as indicated, to similar final temperature.	44

Figure 4.1. Normalized IR T -jump relaxation kinetics of the AK peptide, showing the dependence on T_i . Reprinted with permission from Reference 62 (Huang, C.-Y.; Getahun, Z.; Zhu, Y.; Klemke, J. W.; DeGrado, W. F.; Gai, F. Proc. Natl. Acad. Sci. U.S.A. 2002, 99, 2788-2793). Copyright 2002, Proceedings of the National Academy Sciences.....	67
Figure 4.2. Cartoon illustration of the origin of T_i -dependent conformational relaxation kinetics of an α -helix system.....	68
Figure 4.3. Global fitting results of the CD thermal unfolding curve (A) and the IR T -jump relaxation kinetics (B) of the AK peptide. In each case, the symbols represent the original experimental data and the line corresponds to the respective fit.....	69
Figure 4.4. Conformational distribution of the AK peptide as a function of the number of contiguous helical segments per peptide chain at 0.5 and 14.5 °C, as indicated.....	70
Figure 4.5. Free energy (G) of the AK peptide as a function of its conformation (i.e., the number of peptide units in H state) at 0.5 and 14.5 °C, as indicated. In each case, the line represents the minimum free energy surface.	71
Figure 4.6. Conformational distribution of the AK peptide as a function of the number of peptide units in H state at 0.5, 10.1, and 14.5 °C, as indicated.	72
Figure 4.7. Comparison of equilibrium conformational distributions of the AK peptide at 0.5 and 14.5 °C with the transient conformational distribution obtained at 200 ns along the course of conformational relaxation induced by a T -jump from 0.5 to 14.5 °C.	73
Figure 5.1. The Fourier transform infrared (FTIR) spectrum of AOT surfactant in isooctane	90
Figure 5.2. The FTIR spectrum of Brji30 surfactant in cyclohexane	91
Figure 5.3. The FTIR spectrum of Igepal 520 reverse micelle with $w_0 = 30$	92

Figure 5.4. The FTIR spectrum of LysM in Igepal co-520 reverse micelle of $w_0 = 30$. The absorption from D₂O and Igepal co-520 surfactant is subtracted from the reference compartment of the cell with only D₂O in Igepal co-520 reverse micelle. 93

Figure 5.5. The FTIR spectrum of LEA peptide in AOT reverse micelle of $w_0 = 6$. The absorption contributed by D₂O and AOT surfactant is subtracted from the reference compartment of the cell with only D₂O in AOT reverse micelle. 94

Figure 5.6. The normalized kinetic traces of the probing signal intensity at 1630 cm⁻¹ caused by the change of the temperature in IR *T*-jump experiment. Red line is from D₂O in AOT reverse micelle of $w_0 = 30$ and blue is from bulk pure D₂O. Both traces are from different compartments of a FTIR cell..... 95

Figure 5.7. The FTIR temperature dependence experiment of LysM in AOT reverse micelle of $w_0 = 30$ at amide I' stretching region. 96

Figure 5.8. The kinetic trace of the conformational relaxation process from LysM in Igepal co-520 reverse micelle of $w_0 = 30$. The trace probed at 1630 cm⁻¹ has a T-jump from 40.0 °C to 45.1 °C. The red line is the single-exponential fitting curve with a time constant of 2.3 ms. 97

Figure 5.9. The FTIR temperature dependence experiment of ubiquitin at amide I' stretching region..... 98

Figure 6.1. The fitting of FCS curve from M2TM at pH = 5 where blue line is the overall observable FCS trace, dashed black line is the fitted diffusion component of LUV, green is the overall dynamics subtracted by LUV diffusion, and the red lines are the fitting curves. 112

Figure 6.2. The plot of PET time constant to pH of M2TM with the lipid composition of POPC/POPG/Cholesterol (4/1/2).....	113
Figure 3. The plot of PET time constant to pH of M2TM with the lipid composition of POPC/POPG (4/1)	114
Figure 6.4. The plot of PET time constant to pH of M2TM. Empty circle denotes the experiments from the LUV made of POPC/POPG (4/1) and filled circle shows the experiments from LUV made of POPC/POPG/Cholesterol (4/1/2)	115

LIST OF SCHEMES

- Scheme 4.1. The sequence of the peptide and few conformational states where "P" denotes the peptide group (or the amide unit), the basic unit of the coarse grained model in this study. For each P unit, it can only be in the helical (H) or coil (C) state. The string of P is the coarse grained 1D Ising model, which is aligned to the sequence of the peptide by the dash line indicating the corresponding position of the peptide for each coarse grained unit. 75
- Scheme 4.2. An example of how the free energy of the conformational state is defined where k_1 , k_{-1} , k_2 , k_{-2} , k_3 and k_{-3} are the rate constants for the elemental reaction which are selected from the elemental rate constant set..... 76

LIST of TABLES

Table 3.1. Name and sequence of the peptides studied.	45
Table 3.2. The equilibrium population percentage of each state (F: folded state, I: intermediate state, and U: unfolded state) corresponding to the free energies in Figure 3.2.	46
Table 3.3. T-jump relaxation kinetic parameters calculated for the two three-state folding seniors presented in Figure 3.2.	47
Table 3.4. Relaxation times of BBL obtained from fitting the corresponding <i>T</i> -jump IR relaxation kinetics to a single-exponential function.	48
Table 3.5. Relaxation times of Trpzip-2c obtained from fitting the corresponding <i>T</i> -jump IR relaxation kinetics to a single-exponential function.	49
Table 4.1. Rate constants obtained from the global fitting.	74
Table 6.1. The PET time constants at different pH with the lipid composition of POPC/POPG/Cholesterol (4/1/2).....	116
Table 6.2. The PET time constants at different pH with the lipid composition of POPC/POPG (4/1)	117

CHAPTER 1

Introduction

Conformational dynamics studies on biomolecules have gained an explosive growth over the past 50 years since the first crystal structures of myoglobin and DNA were published in the 1950s.¹⁻³ The reason that conformational dynamics studies of the biomolecules started almost at the beginning of structural biology is that the mechanisms of protein biological functions cannot be fully understood with only their structures. Although technology has advanced tremendously during these years; for example, (1) the time resolution of time-resolved spectroscopy reached femtosecond timescales, (2) single molecule measurements could be compared with conventional ensemble measurements due to the development of highly sensitive detectors, and (3) nonlinear multidimensional spectroscopy was invented, the conformational dynamics of biomolecules is still very challenging due to the size of molecule, and the complicated intra- and intermolecular interactions. To understand the conformational dynamics of protein folding, one must obtain the free energy potential surface of the biomolecule; however, it is almost impossible to obtain a high dimensional free energy potential using current experimental techniques. Therefore, approximations that can coarsely grain the molecule to reduce the number of degrees of freedom and reduce the dimensionality of the surface have become important strategies to study the conformational dynamics. Based on those strategies, this thesis is focused on the conformational dynamics of proteins from the folding dynamics of the one-state BBL peptide and alanine-based helical peptides to the proton conduction of the Influenza A M2 proton channel.

The issue of protein folding has now advanced to a stage where diversity in the folding mechanism is inevitable. To match the fast expanding knowledge of proteins, many models of the folding process are developed. The two-state model of folding is the

most common folding mechanism. It was developed early in the study of protein folding. It is popular because it simplifies the folding mechanism into a unimolecular reaction with an energy barrier between the initial (unfolded) and final (folded) states. The three-dimensional protein structure is a product of sidechain packing and backbone-backbone hydrogen bonding. However, assuming that all the hydrogen bonds can break and form simultaneously in a folding process may not be suitable in all cases. Exceptions to two-state model of folding are expected and have been observed.⁴⁻¹¹

Around twenty years ago, Wolynes *et al.* introduced the idea of a downhill (one-state) folding mechanism from energy landscape theory.¹² In the downhill scenario, the energy potential surface is represented as a barrierless single well, which allows for many conformations of the protein to be populated.¹³⁻¹⁵ The corresponding biological significance of the downhill scenario can be illustrated by the idea of a molecular rheostat.^{5, 16-17} From the view point of evolution, the nature of the downhill mechanism allows both protein stability and flexibility to be satisfied. This meets the demands of biological processes such as proteolytic degradation of regulatory proteins.¹⁸ There is an increasing number of protein folding studies proposing that the energy determined assuming a two-state model is small and the downhill model is more applicable.

In chapter 3, we study the folding mechanism of BBL, the peripheral subunit of the binding domain in 2-oxoglutarate dehydrogenase of *Escherichia coli*, which is reported as the first downhill folder in 2002.⁵ Unlike the intrinsic difference between the two-state and downhill models, both models have similar experimental behaviors. They give sigmoidal melting curves in temperature-dependent experiments. The relaxation traces of downhill folders can also follow an exponential function like two-state folders.¹⁹

Although there are many debates on the existence of downhill folders, several experimental signatures cannot be explained by the two-state mechanism such as BBL and other potential downhill folders.²⁰⁻²⁵ Probe-dependence¹⁷ is one of the useful ways to differentiate the downhill model from the two-state model.^{5, 17} Since different probes perturb the system differently, probe-dependence sometimes can be criticized as the outcome of the choice of the probes.^{20, 26} Directly from the intrinsic amide I stretching, a new experimental signature in the dynamics of downhill folders is described in this study.

The α -helix is one of the basic building blocks in protein secondary structure. The importance of α -helices cannot be addressed too much in the study of protein folding. Such an abundant secondary structure of proteins actually reveals the folding dynamics which is non-trivial. Few studies have shown that the folding process of α -helices in alanine-based peptides does not follow the classic two-state model.²⁷⁻²⁸ Alternatively, the helix-coil folding dynamics is commonly used to explain the folding process of the α -helix.²⁹⁻³¹ The nucleation and propagation rates of the helix-coil dynamics become the key to allowing the folding process of an α -helix to be fundamentally studied. However, experimentally accessing the nucleation and propagation rates still remains a challenge. Few molecular simulation studies show their attempts to obtain the nucleation rates, but the reported rates spread out in a wide time scale.³²⁻³⁶ Some of the groups introduce additional energy transfer probes to the helical structure and obtain the rates indirectly.³⁷⁻³⁹ A straightforward method which directly determines the nucleation and propagation rates is still in need.

In chapter 4, we present a new method to directly extract the nucleation and propagation rates by fitting the experimental kinetic traces with our kinetic model, which is based on the helix-coil transition theory.

Reverse micelles have become the useful systems to study water molecules at the interfacial region and protein loaded confined environment. In this study, we first combine an IR T -jump experiment with reverse micelles to extend the measuring time of the T -jump experiment. With the extended measuring time of the T -jump experiment, the gap in the measuring time range between the T -jump experiment and stopped-flow experiment can be overcome.

In chapter 5, both anionic and non-ionic surfactants are studied to better understand the electrostatic interaction between the protein and the surfactant layer of reverse micelles. The positively charged LysM is loaded into the non-ionic Igepal co-520 reverse micelle to study the folding dynamics. The conformational relaxation is determined to be 2.3 ms at 40 °C. Ubiquitin loaded into the negatively charged AOT reverse micelles reveals the unusual formation of aggregation. The LEA peptide is loaded into low w_0 reverse micelles to study the folding dynamics induced by dehydration, but limited information is obtained due to the low T -jump with the small sized reverse micelle.

Due to the threat of public health from the Influenza A virus, understanding the mechanism of how the virus invades the host cell becomes critical to developing anti-influenza treatments. One strategy of anti-influenza treatments is to block the function of the Influenza A M2 proton channel (AM2). One function of AM2 is to conduct protons

from the endosome lumen to the virus envelope during the viral invasion. However, the mechanism of the proton conduction of AM2 is still unclear. Previous studies of AM2 have provided insight into the structure of AM2 in the closed form, the roles of the gating residues, His37 and Trp41, the possible binding sites of the anti-influenza A drugs, and the kinetics of proton conduction. However, dynamics studies of AM2, which are crucial to understanding the conduction mechanism, are rarely done.

In chapter 6, we use photoinduced electron transfer fluorescence-quenching correlation spectroscopy (PET-FCS) to study the conformational dynamics of the AM2 transmembrane region. The time constant of the inter helix motion is first reported along with the transition between the closed and open states, providing a new overall understanding of the proton conduction of AM2.

CHAPTER 2

Methods

2.1 Circular Dichroism (CD) Spectroscopy

CD spectroscopy is one of most common tool to study the secondary structure of protein. CD spectroscopy is a type of UV/Vis absorption spectroscopy that measures the difference of the absorbance between the left-handed and right-handed polarized light. Only chiral molecules would show preferred absorption on one of the polarized lights. Therefore, it is useful to probe the secondary structure of proteins. Since CD spectroscopy is based on UV/Vis absorption, the probe studied by CD spectroscopy must involve the electronic transition. The C=O group of a protein is the ideal group to study the secondary structure of proteins. The electronic transitions of C=O are from n to π^* and π to π^* corresponding to the range from 190 nm to 250 nm. Due to the unique 3-D chiral structures of protein secondary structures, each of them has its own signature of CD spectroscopy. α -helical structure has two minima at 222 nm and 209nm, β -sheets have one minimum at ~215 nm, and the coil structure has one minimum at ~195 nm. Although each secondary structure has its unique CD spectrum, limited information about the secondary structure can be obtained when there is the combination of different secondary structures.

2.2 Fourier-Transform Infrared (FTIR) Spectroscopy and IR Spectroscopy of Proteins

FTIR spectroscopy measures the absorption due to the vibrations of molecules. For conventional FTIR, a broad band of light (from 500 cm^{-1} to 4000 cm^{-1}) is sent through the interferometer to obtain the interferogram of the light. After a Fourier

transform, the interferogram of the light is converted into a frequency-domain transmittance spectrum. The transmittance spectra collected at the sample cell and the reference cell can be further converted into the absorption spectrum by using Beer's law.

$$A = -\log\left(\frac{I_s}{I_r}\right)$$

where A is the absorbance, I_s is the transmitted intensity at sample cell, and I_r is the the transmitted intensity at reference cell. In our setup, there are two compartments on the spacer, and both the sample measurement and reference measurement can be done in one cell.

For IR spectra of proteins, the amide I stretching mode (from 1620 cm^{-1} to 1680 cm^{-1}) is mostly used to study the secondary structure of the protein. It is treated as the intrinsic probe for the secondary structure, and is sensitive to the local environment. Due to the difference between different secondary structures, the amide I stretching has (1) one band at $1640\text{-}1650\text{ cm}^{-1}$ for an α -helix, (2) one narrow band at 1620 cm^{-1} for parallel β -sheets, (3) one band at 1630 cm^{-1} and a weak band at 1680 cm^{-1} for anti-parallel β -sheets, (4) a broad band centered at 1650 cm^{-1} for coil structure. Although the amide I stretching mode is a global probe for protein secondary structures, it can also be used to study the local environment of the protein. Isotope labeling of the amide group has become a useful tool to change the amide I stretching mode into a local probe. Isotope

labeling of ^{13}C and ^{18}O on the C=O group of amide results in the red shift of the amide I band ($\sim 50\text{ cm}^{-1}$ for ^{13}C and $\sim 70\text{ cm}^{-1}$ for ^{13}C and ^{18}O together). The red-shifted band is then used to study the local environment of the protein.

2.3 Laser-Induced Temperature-jump (*T*-jump) Spectroscopy

The *T*-jump experiment is popular for studying the relaxation process due to the fast jump of the temperature. By applying a *T*-jump experiment to protein, the relaxation trace from the *T*-jump experiment can be used to study the folding dynamics of the protein. In the conventional IR pump IR probe *T*-jump experiment, a nanosecond IR pumping laser pulse is sent to heat up water in the sample within several nanoseconds with an increase of $\sim 15\text{ }^\circ\text{C}$ in temperature. The continuous-wave (CW) IR probing laser is sent through the center of the pumping area to probe the optical density change caused by the incoming pumping laser pulse. Water is usually replaced by deuterium oxide (D_2O) to avoid the saturation in probing frequencies, since the strong absorption of the water vibrational bending mode occurs at 1643 cm^{-1} . Both D_2O and the conformational dynamics of the protein can contribute to the change in optical density ($\Delta\text{ O. D.}$) at the probing frequency. The change contributed by D_2O can be subtracted by $\Delta\text{ O. D.}$ of the reference cell with pure D_2O . After subtraction $\Delta\text{ O. D.}$ only consists of the conformational dynamics of the protein which would reflect the conformational relaxation corresponding to the jump in temperature. The temperature dependence of optical density of water is further used as an internal thermometer by converting $\Delta\text{ O. D.}$

of D₂O at the reference cell into the corresponding temperature change in the T -jump experiment.

2.2 Fluorescence Correlation Spectroscopy (FCS)

By using FCS, the diffusion coefficient can be used as a probe to study the conformational change of the protein. The setup of FCS is based on the setup of confocal microscopy. A continuous-wave laser is used for the excitation of the fluorescent probe, and the emission collected by the objective of the microscope goes through a pinhole with a 60 μm diameter before reaching the detector. With the pinhole, only the emission from the confocal volume (~ 1 femtoliter) would be collected by the detector. The detector records the intensity trace of the emission from the confocal volume. The output intensity trace is further correlated to itself to show the correlation spectroscopy. By fitting the correlation curve to the corresponding diffusion model (see the equation below), the diffusion time of the sample can be extracted. To convert the diffusion time into the corresponding diffusion coefficient, the radial radius of the confocal volume is first determined by a standard with known diffusion coefficient, and then used to calculate the diffusion coefficient of the probed molecule.

$$G(\tau) = \frac{1}{N} \cdot \left(\left(\frac{1}{1 + \frac{\tau}{\tau_D}} \right) \cdot \left(\frac{1}{1 + \frac{\tau}{\omega^2 \tau_D}} \right)^{1/2} \right) \times \left(\frac{1 - \sum_{i=1}^m \left(T_i - T_i \cdot \exp\left(-\frac{\tau}{\tau_i}\right) \right)}{1 - \sum_{i=1}^m T_i} \right)$$

$$\omega = \frac{\omega_z}{\omega_{xy}}$$

$$D = \frac{\omega_{xy}^2}{4\tau_D}$$

where τ_D is the 3-D diffusion time constant, ω is the axial- to lateral-dimension ratio of the confocal volume (ω_z / ω_{xy}), N is the number of fluorescent molecules in the confocal volume, τ_i and T_i are the respective time constant and amplitude of the dynamics component i , and D is the diffusion coefficient.

CHAPTER 3

Using VIPT-Jump to Distinguish Between Different Folding

Mechanisms: Application to BBL and a Trpzip

Reprinted with permission from Journal of American Chemical Society, Chun-Wei Lin, Robert M. Culik, and Feng Gai, (2013) 135, 7668-7673. DOI: 10.1021/ja401473m, <http://dx.doi.org/10.1021/ja401473m>,⁴⁰ Copyright (2013) American Chemical Society.

3.1 Abstract

Protein folding involves a large number of sequential molecular steps or conformational substates. Thus, experimental characterization of the underlying folding energy landscape for any given protein is difficult. Herein, we present a new method that can be used to determine the major characteristics of the folding energy landscape in question, e.g., to distinguish between activated and barrierless downhill folding scenarios. This method is based on the idea that the conformational relaxation kinetics of different folding mechanisms at a given final condition will show different dependences on the initial condition. We show, using both simulation and experiment, that it is possible to differentiate between disparate kinetic folding models by comparing temperature jump (*T*-jump) relaxation traces obtained with a fixed final temperature and varied initial temperatures, which effectively varies the initial potential (VIP) of the system of interest. We apply this method (hereafter refer to as VIPT-jump) to two model systems, tryptophan zipper (Trpzip)-2c and BBL, and our results show that BBL exhibits characteristics of barrierless downhill folding, whereas Trpzip-2c folding encounters a free energy barrier. In addition, using the *T*-jump data of BBL we are able to provide, via Langevin dynamics simulations, a realistic estimate of its conformational diffusion coefficient.

3.2 Introduction

Protein folding involves many degrees of freedom or conformational substates and, therefore, represents a hyperdimensional problem.^{12, 15, 41} However, in practice the folding free energy landscape is often projected onto a low dimensional space, e.g., as a function of a putative ‘folding’ coordinate. As shown (Figure 3.1), in the case of a one-dimensional folding coordinate, various folding scenarios can, in principle, be differentiated by the number, position, and magnitude of the free energy barriers that separate the folded state from the unfolded conformational ensemble. For example, two limiting cases become apparent: One contains a single free energy barrier that separates the folded from the unfolded state, i.e., the two-state folding mechanism (Figure 3.1A), whereas the other involves a continuum of thermally accessible states, i.e., the downhill or one-state folding scenario (Figure 3.1D).^{6, 14-15, 18, 42-46} Other simple cases involve one or more observable intermediate states, which can be located on either side of the major folding barrier (Figure 3.1B,C). While a onedimensional representation of the protein folding free energy landscape is informative and practical, for a given protein the existing experimental methods for studying folding kinetics sometimes cannot distinguish between different folding scenarios. For example, it has been shown that both two-state and downhill folding mechanisms can yield folding kinetics that are essentially indistinguishable by conventional experimental techniques.⁴⁷⁻⁴⁸ While these two folding scenarios, which are polar opposites, can be distinguished from each other by whether their folding kinetics^{10, 49-50} and/or thermodynamics²³ depend on the conformational probe, we still lack a more straightforward approach to characterize the underlying nature of the folding free energy surface of the protein in question. Herein we show, for a given

final temperature in a temperature jump (T -jump) relaxation experiment,⁵¹⁻⁵⁴ that by varying the initial temperature, which is equivalent to varying the initial potential of the system in question, the difference in the resulting relaxation kinetics reveals the nature of the underlying folding free energy landscape of the target protein. While the strategy of varying T -jump amplitude has been employed before in protein folding studies,^{49, 55-59} to the best of our knowledge it has not been used to characterize the underlying folding free energy landscape. Specifically, we apply this VIPT-jump technique to two model systems, tryptophan zipper (Trpzip)-2c and BBL, and our results show that the folding kinetics of Trpzip-2c are consistent with an activated folding mechanism, while those of BBL are characteristic of a barrierless downhill folder. In addition, using the free energy surface of BBL determined by Wang and co-workers⁶⁰ and Langevin dynamics (LD) simulations, we are able to extract the conformational diffusion coefficient of BBL from the experimentally measured conformational relaxation kinetics.

3.3 Results and Discussion

For a two-state folding scenario (Figure 3.1A), it is easy to show that the population redistribution kinetics, e.g., in response to a T -jump, only depend on the final temperature and not the initial temperature, whereas the latter determines the amplitude of the probing signal. Similarly, for folding mechanisms involving an intermediate state, populated at either the left- or right-hand side of the major folding free energy barrier (Figure 3.1B,C), it is easy to show that the population relaxation kinetics of the folded/ unfolded state, in response to a T -jump, are biphasic with two relaxation time constants determined by the corresponding microscopic rate constants at the final temperature. Thus, in this case the measurement of relaxation kinetics alone is insufficient to differentiate between the two scenarios. On the other hand, we show that the VIPT-jump technique is able to do so, which complements other methods.⁶¹⁻⁶² The applicability of this method simply stems from the fact that for such reversible ‘reaction’ systems, the relative amplitudes of the two kinetic phases (for a given final temperature) depend on the initial population distribution or temperature. To further illustrate this point, an example is given below. For the two folding pathways presented in Figure 3.2, it is easy to show that for pathway A the relative amplitude of the fast phase of the population relaxation kinetics of the folded state (F), at a final temperature (T_f) of 323.0 K, is increased from 8.9 to 16.1% when the initial temperature (T_i) is changed from 310.5 to 298.0 K, whereas the relaxation kinetics of the unfolded state (U) are essentially single exponential, and that for pathway B it is the relaxation kinetics of U that are sensitive to T_i (e.g., the relative amplitude of the fast phase is decreased from 30.8% to 25% in this case) (Tables 3.2, 3.3 and Figure 3.2). Thus, taken together, this simple numerical analysis illustrates the utility

of the VIPT-jump method in distinguishing between folding pathways that conventional kinetics measurements cannot. In principle, the utility of the VIPT-jump technique is not only limited to these classical models but also can be further applied to the downhill folding scenario. For a population redistribution process occurring on a free energy surface that does not contain an appreciable barrier between states (Figure 3.1D), evaluation of the relaxation kinetics is less straightforward. Herein, we employ LD simulations to determine how the population relaxation kinetics at a given final temperature depend on the initial temperature, assuming that the dynamics occur in the overdamped regime.^{11, 63-64} Specifically, the time-dependent population distribution function, $P(t,q)$, is obtained by numerically solving the following equation for each molecule:⁶⁵

$$\frac{k_B T}{D(T)} \frac{dq}{dt} = -\frac{dG(q,T)}{dq} + \Gamma(t) \quad (1)$$

where $G(q,T)$ is the one-dimensional free energy surface, q the folding coordinate, $D(T)$ the diffusion coefficient, T the absolute temperature, and k_B the Boltzmann constant. In addition, $\Gamma(t)$ represents the random force arising from the underlying thermal bath with a mean value of 0 and a normally distributed variance that is bounded by the fluctuation – dissipation theorem.⁶⁶ In the present study, the variance of $\Gamma(t)$ is set to be $2(k_B T)2\delta(t)/D$, where $\delta(t)$ is the delta function corresponding to a Markovian process.⁶⁶ In reality, the diffusion coefficient, D , may show a dependence on q ; for simplicity in the present study we have assumed that it only depends on temperature. In practice, it is common to choose one of the protein’s structural parameters as the folding coordinate q , such as the fraction of native contacts (Q), the radius of gyration (R_g), or the root-mean-

square distance (rmsd), which measures the displacement of each atom in a given structure from its native position. While the choice of the folding coordinate and the exact shape of the one-dimensional downhill folding free energy surface do not change our conclusions, in the present study we used the folding free energy surface determined by Wang and co-workers²⁶ for BBL as a reference to determine $G(q,T)$. Based on extensive molecular dynamics (MD) simulations and analyses using the weighted histogram analysis method, Wang and co-workers²⁶ were able to extract an effective folding free energy surface as a function of rmsd at 298 K. To determine $G(q,T)$ at other temperatures, we simply tilted the free energy surface obtained by Wang and co-workers. Specifically, the degree of tilting for any given temperature is determined by the criterion that the average nativeness of the protein at the target temperature matches that estimated from the circular dichroism (CD) temperature melting curve of BBL (see Supporting Information).

To determine whether the kinetics of a T -jump induced population redistribution process on a one-dimensional downhill- like folding free energy surface are sensitive to the initial temperature, we carried out two LD simulations that differ only in the initial population distribution. Specifically, we first determined three free energy surfaces using the method discussed above at three temperatures, e.g., 310.15 (T_f), 303.15 (T_{i1}), and 298.15 K (T_{i2}). We then used these free energy surfaces, i.e., $G(q,T_f)$, $G(q,T_{i1})$, $G(q,T_{i2})$, to determine the corresponding equilibrium (or Boltzmann) population distributions, i.e., $P_{eq}(q,T_f)$, $P_{eq}(q,T_{i1})$, and $P_{eq}(q,T_{i2})$. In the next step, we carried out LD simulations to determine the population relaxation dynamics, i.e., $P(t,q)$, using the following conditions: $P(t = 0,q) = P_{eq}(q,T_{i1})$ or $P(t = 0,q) = P_{eq}(q,T_{i2})$ and $P(t \rightarrow \infty,q) = P_{eq}(q,T_f)$. Finally,

following Gruebele and coworkers,⁶³ we converted $P(t,q)$ to a signal, $S(t)$, using the following equation:

$$S(t) = \int H(q - q_{q^*}) p(t, q) dq \quad (2)$$

where H is the Heaviside function, i.e., $H = 1$ when $q \geq q^*$ and $H = 0$ when $q < q^*$. While the exact value of q^* may well depend on the nature and location of the conformational probe used in a specific experiment, without loss of generality in the current study, we have assumed that q^* corresponds to an rmsd of 3.36 Å, which is equivalent to a nativeness of 0.7. While this choice is somewhat arbitrary, it does not change the conclusions reached below. In addition, when the amide I band of the protein in question is used to probe conformational relaxation (see below), the use of a heaviside step function to extract the signal, $S(t)$, from the time-dependent population distribution function is a reasonable approximation. As shown (Figure 3.3), the results obtained from LD simulations confirm our expectation that for a T -jump induced population relaxation process occurring on a barrier-less free energy surface, the relaxation dynamics depend not only on T_f but also on T_i , which determines the initial equilibrium population distribution. In addition, consistent with several previous studies⁴⁷⁻⁴⁸ the relaxation traces in Figure 3.3 can be well described by a single-exponential function (Figure 3.11), indicating that in order to uncover the true nature of the underlying folding energy landscape of the protein in question, one cannot simply rely on conventional relaxation kinetics measurements. Thus, taken together, these simulation results provide concrete evidence in support of the applicability of the VIPT-jump method in distinguishing between various protein folding mechanisms, especially between two-state and

barrierless downhill folding scenarios. Additional simulations indicate that even for a folding free energy barrier as small as $1.5 k_B T$, the population relaxation kinetics show no measurable dependence on initial temperature, further underscoring the sensitivity of this method.

To further test the utility of the VIPT-jump method, we applied it to two model systems, BBL and Trpzip-2c. We chose BBL because various experimental^{5, 17, 23, 26, 67} and computational^{48, 60, 68-73} studies have suggested that its folding encounters a negligible barrier, whereas Trpzip-2 folding has been shown in several studies to involve a free energy barrier.⁷⁴⁻⁷⁸ Additionally, BBL folds on a similar time scale to Trpzip-2c,^{21, 78} making the comparison more reliable. Specifically we measured the T -jump induced population relaxation kinetics of both systems based on the protocol of the VIPT-jump method, using timeresolved infrared (IR) spectroscopy and probing frequencies within the amide I band of these polypeptides. The amide I band of proteins/peptides arises predominantly from the stretching vibrations of backbone carbonyls and is a sensitive IR reporter of protein secondary structural contents.⁷⁹

As shown (Figures 3.8 and 3.10) and consistent with previous studies,^{5, 26} the CD thermal unfolding curve of BBL indicates that increasing the temperature from 30 to 65 °C induces a significant change in the secondary structural content of the protein and that the apparent melting temperature (T_m) is ~ 44 °C. Thus, we carried out a series of T -jump IR measurements on BBL with final temperatures falling within this temperature range. In addition, we used probing frequencies of 1630 and 1668 cm^{-1} . As shown (Figure 3.12), the amide I' band (amide I in D_2O) of BBL decreases in intensity at 1630 cm^{-1}

with increasing temperature, corresponding to a loss of helical structures, while there is a concomitant gain in intensity at 1668 cm^{-1} , corresponding to an increase in disordered conformations. Thus, measurements at each of these frequencies provide representative tests of the sensitivity of the VIPT-jump method. As shown (Table 3.11), the T -jump relaxation kinetics obtained with both probing frequencies and at all the final temperatures tested show a certain dependence on the initial temperature. In particular, as indicated (Figures 3.4 and 3.5), while these relaxation traces can be fit by a single-exponential function, their overall relaxation kinetics, obtained at a given T_f , show a T_i dependence with a relationship that a larger T -jump amplitude results in a faster relaxation rate. This is consistent with the LD simulation results for a downhill folder shown above (Figure 3.3), where a larger T -jump also leads to a faster relaxation, due to a greater force acting on the initial population ensemble. On the other hand, due to the free energy barrier present in its folding pathway, we expect that the relaxation kinetics of Trpzip-2c will not show a similar dependence. Indeed, as shown (Figures 3.6 and 3.16), two T -jump IR relaxation traces obtained at the same final temperature ($61.8\text{ }^\circ\text{C}$) but with different initial temperatures (46.8 and $52.8\text{ }^\circ\text{C}$) are indistinguishable within our experimental errors, indicating that the population relaxation rate of this peptide depends only on the final temperature, characteristic of an activated folding mechanism. Taken together, these results provide a direct validation of the utility of the VIPT-jump method in revealing the nature of the protein folding energy landscape and, especially, its ability to distinguish between barrier-crossing and barrierless folding mechanisms.

Our results provide additional evidence to support the notion that the folding of BBL, at least under our experimental conditions, does not encounter a significant free

energy barrier.^{5, 17, 23, 26, 48, 60, 67} Thus, its folding process can be treated as a diffusive motion along the folding coordinate, and as such, the T-jump induced relaxation kinetics of BBL can be used, in conjunction with LD simulations, to estimate its conformational diffusion coefficient as well as the ruggedness of its potential energy surface. Because, as indicated in eq 1, the population relaxation kinetics depend on both $G(q,T)$ and $D(T)$, one needs to know $G(q,T)$ in order to accurately extract $D(T)$ from the T-jump experimental data. In principle, one could globally analyze all of the thermodynamic data (e.g., that obtained from CD or IR measurements) and T-jump relaxation kinetics obtained at different temperatures to simultaneously determine, in a self-consistent manner, $G(q,T)$ and $D(T)$. However this is beyond the scope of the present paper, so instead we use the $G(q,T)$ of Wang and co-workers⁶⁰ to provide an estimate of the conformational diffusion coefficient of BBL near its T_m . As shown (Figure 3.7), the T-jump induced relaxation kinetics obtained at 46.8 °C (T_f) can be well described by a population redistribution process via conformational diffusion on the corresponding free energy surface; the diffusion coefficients thus obtained (i.e., $3.3 \times 10^5 \text{ nm}^2/\text{ns}$ for $T_i = 38.1 \text{ °C}$ and $2.7 \times 10^{-5} \text{ nm}^2/\text{ns}$ for $T_i = 41.1 \text{ °C}$) show a dependence on the initial temperature. This T_i dependence is expected, as the conformational diffusion coefficient depends not only on the final temperature but also on the folding coordinate,⁶⁰ a condition not explicitly considered in the current simulations. Nevertheless, the values of these diffusion coefficients are in quantitative agreement with the diffusion coefficient obtained by Gruebele and co-workers¹⁰ for a mutant of λ repressor ($3 \times 10^{-5} \text{ nm}^2/\text{ns}$). Because λ repressor has approximately twice as many residues as BBL, this agreement suggests that the conformational diffusion of other proteins may have a similar diffusion coefficient.

For example, a simple calculation using this value of D suggests that it takes ~ 30 ns to elongate an α -helix by one turn (3.5 residues), via a conformational diffusion search process. This rate of helix propagation is entirely consistent with those estimated from experimental measurements.^{38, 80-81}

3.4 Conclusion

It is apparent that the free energy of a protein system (including solvent) depends on many degrees of freedom, which collectively determine the conformational state of the protein. However, when folding or unfolding is monitored with a specific experimental probe, such as CD, IR, or fluorescence, it often exhibits simple kinetics (e.g., one or two exponentials). Moreover, and perhaps more importantly, different folding scenarios, e.g., the two-state and downhill mechanisms, can give rise to practically indistinguishable kinetics, making it difficult, if not impossible, to elucidate the nature of the underlying folding energy landscape based on conventional kinetics measurements. Herein, we show, by varying the initial temperature in a T -jump experiment, which essentially varies the initial potential (VIP) of the protein system in question, that it is possible to discriminate between different types of folding mechanisms. This VIPT-jump method is akin to the strategy used in electronic spectroscopy to create different Franck–Condon states on the excited electronic potential energy surface by using different excitation wavelengths. Experimentally, we apply this VIPT-jump method to two model systems, BBL and Trpzip-2c, which have been suggested to follow two different folding mechanisms (i.e., downhill versus activated). We find that the T -jump induced conformational relaxation kinetics of BBL, but not Trpzip-2c, show dependence on the initial temperature at a fixed final temperature, with a larger T -jump resulting in a faster relaxation rate. These findings provide additional evidence to support the idea that BBL is a downhill folder. In addition, using LD simulations we are able to extract an apparent conformational diffusion coefficient for BBL, the magnitude of which is in agreement with that determined for another downhill

folder, λ repressor. An exciting new direction for this method would be to use VIPT-jump to study the free energy landscapes of intrinsically disordered proteins, which currently are relatively unknown.

3.5 Experimental Section

BBL and Trpzip-2c were synthesized on a PS3 automated peptide synthesizer (Protein Technologies, MA) using standard Fmoc protocols. Peptide products were further purified by reverse-phase chromatography and identified by matrix-assisted laser desorption ionization mass spectroscopy. Trifluoroacetic acid (TFA) removal and D_2O exchange were achieved by multiple rounds of lyophilization.

All peptide samples were prepared in 20 mM phosphate buffer solution (pH 7), and the peptide concentrations were in the range of 45 μM for CD and 4 mM for IR measurements. The details of all spectroscopic measurements, including the T-jump IR setup, have been described elsewhere.⁸² Specifically, for the VIPT-jump experiments, variation of the *T*-jump magnitude was achieved by appropriately adjusting the pump intensity using a neutral density filter (Schott Glass Technologies, Inc., PA) and the initial temperature. For each *T*-jump relaxation trace obtained, the corresponding final temperature was measured twice, before and after the experiment, using the absorbance change of D_2O in the reference side of the IR cell.⁸² If the final temperature deviated by more than 0.5 °C from the targeted value, the corresponding kinetic trace was discarded.

CD spectra and thermal melting curves were obtained on an Aviv 62A DS spectrometer (Aviv Associates, NJ) with a 1 mm sample holder. Fourier transform infrared (FTIR) spectra were collected on a Magna-IR 860 spectrometer (Nicolet, WI) using a homemade, twocompartment CaF_2 sample cell of 56 μm path length.

Langevin dynamics simulations were performed using Matlab (The MathWorks, MA) and a time step of 35 ns, and integration was performed using Runge-Kutta methods.

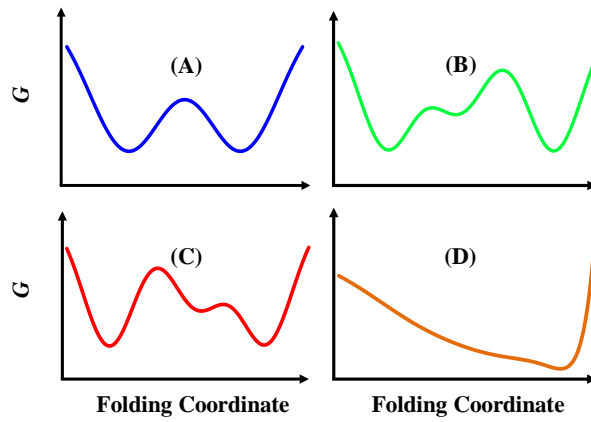


Figure 3.1. Cartoon depiction of representative folding free energy surfaces. (A) two-state folding scenario, (B) and (C) three-state folding scenarios with the observable intermediate state located on either side of the major folding barrier, and (D) downhill or one-state folding scenario.

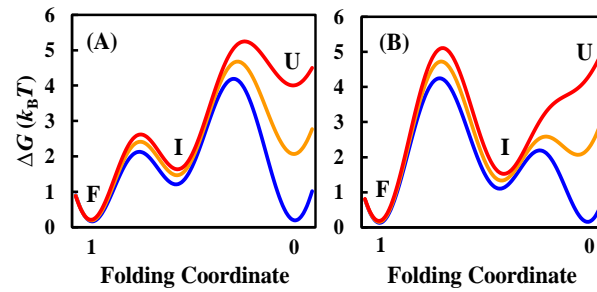


Figure 3.2. Relative free energies of U, I, and F in a three-state folding scenario at 298.0 (red), 310.5 (orange), and 323.0 K (blue), respectively, with the intermediate state located at either the left- (A) or right-hand (B) side of the major folding free energy barrier.

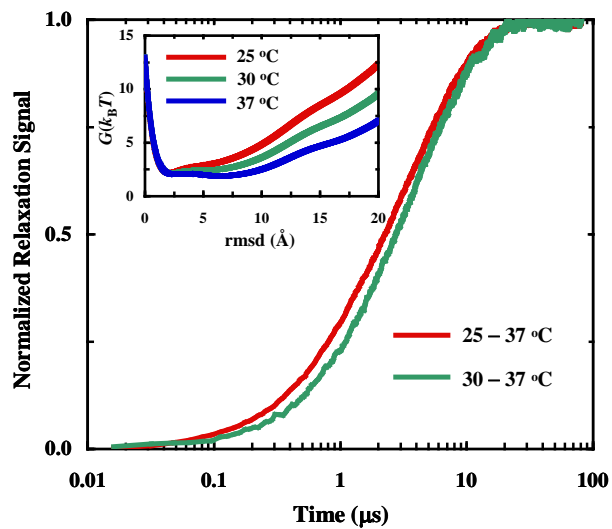


Figure 3.3. Simulated relaxation kinetics in response to T -jumps from different initial temperatures to the same final temperature, as indicated, obtained via LD simulations using the free energy surfaces shown in the inset.

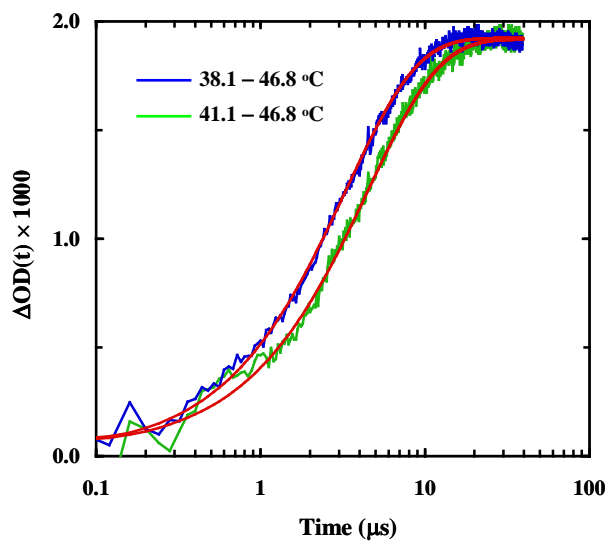


Figure 3.4. Comparison of the normalized conformational relaxation kinetics of BBL obtained with a probing frequency of 1668 cm^{-1} and at a final temperature of $46.8\text{ }^{\circ}\text{C}$, from two different initial temperatures, as indicated. The red lines are fits of the data to a single-exponential function, and the resulting time constants are reported in Table 3.4.

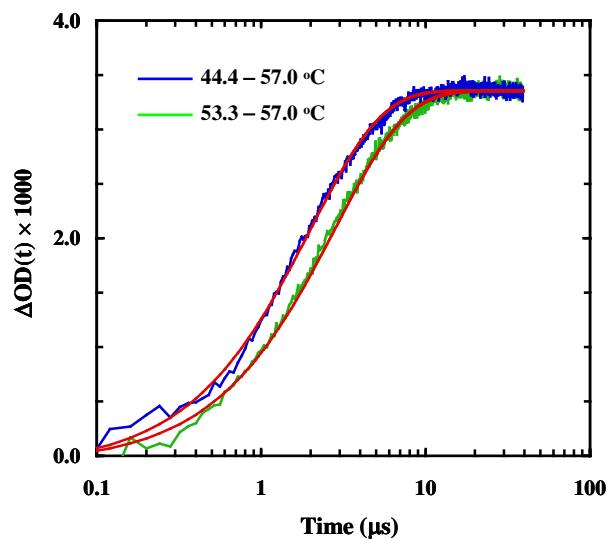


Figure 3.5. Comparison of the normalized conformational relaxation kinetics of BBL obtained with a probing frequency of 1668 cm^{-1} and at a final temperature of $57.0\text{ }^{\circ}\text{C}$, from two different initial temperatures, as indicated. The red lines are fits of the data to a single-exponential function and the resulting time constants are reported in Table 3.4.

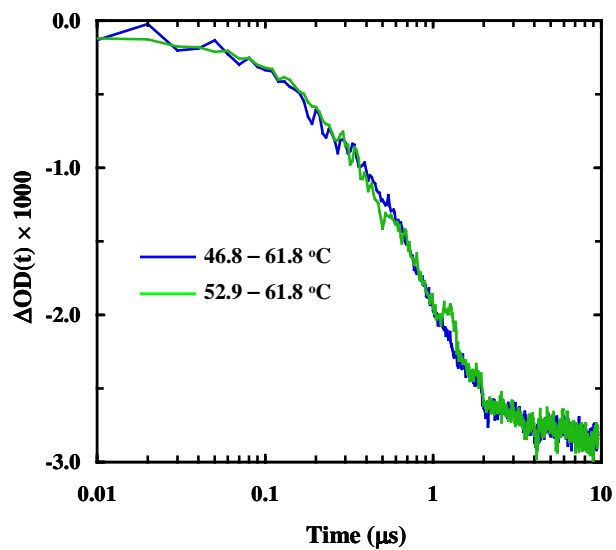


Figure 3.6. Comparison of the normalized conformational relaxation kinetics of Trpzip-2c obtained at a final temperature of 61.8 °C, from different initial temperatures, as indicated. The probing frequency was 1630 cm^{-1} .

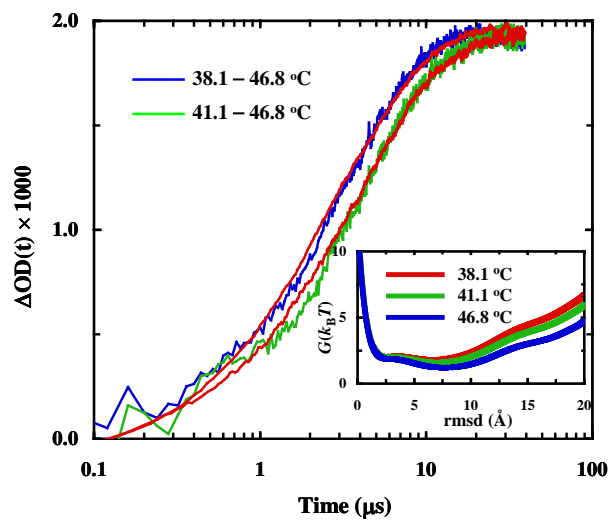


Figure 3.7. LD fits (red) of the experimental IR relaxation kinetics of BBL from Figure 3.4, using the free energy surfaces shown in the inset. The resulting effective conformational diffusion coefficients are given in the text.

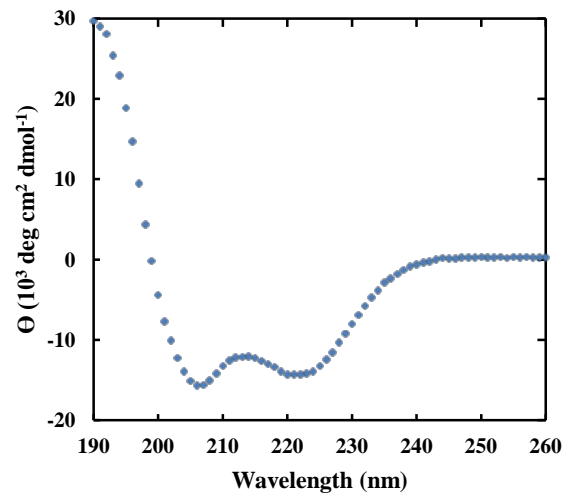


Figure 3.7. Far-UV CD spectrum of BBL, collected at 1°C.

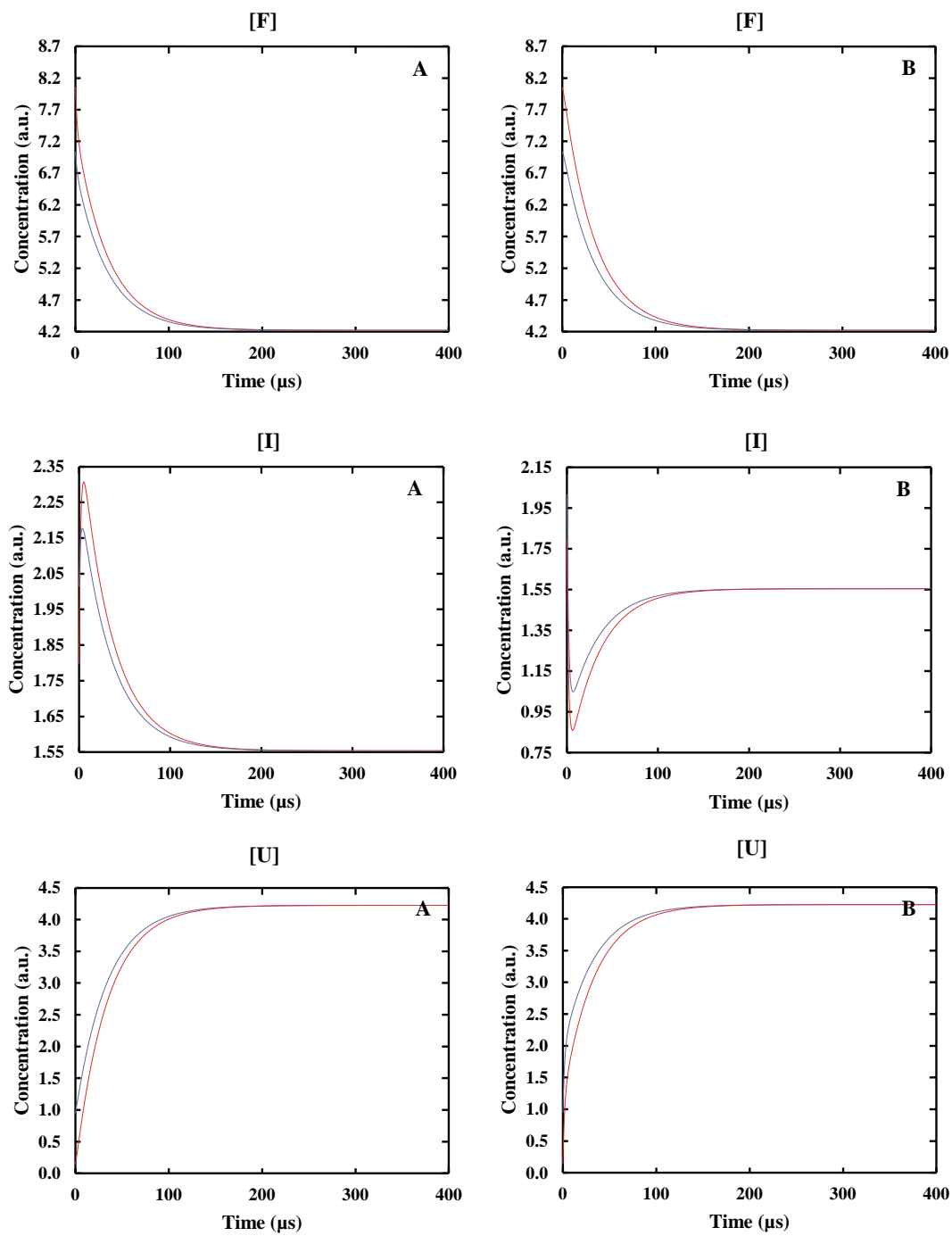


Figure 3.9. Relative population changes in response to a T -jump of 298 to 323 K (red) or 310.5 to 323 K (blue), for the two three-state folding mechanisms (A or B, as indicated) presented in Figure 3.2.

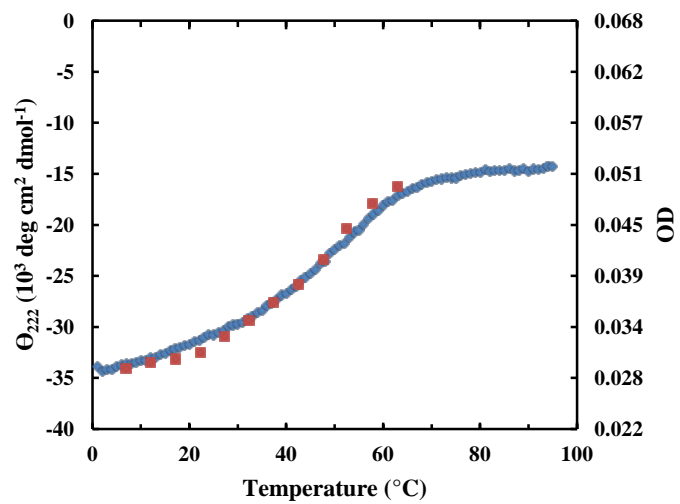


Figure 3.10. Overlay of CD thermal melting curve of BBL (blue) with IR melting curve probed at 1668 cm^{-1} (red).

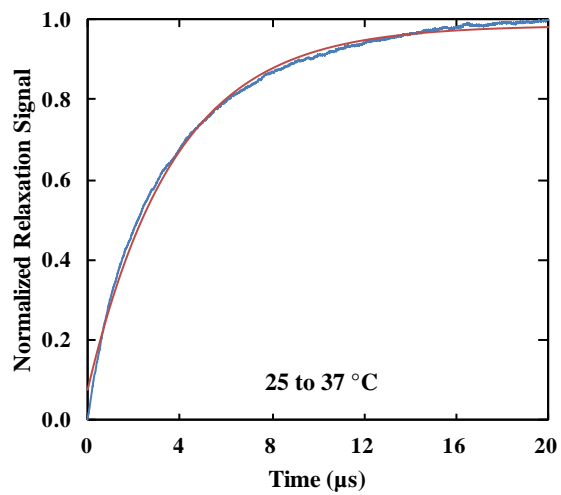
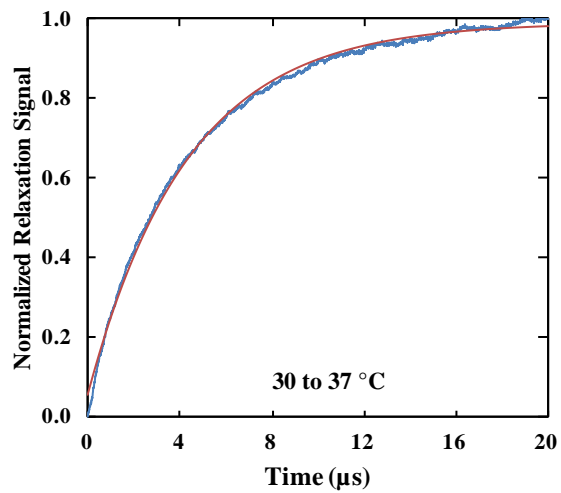


Figure 3.11. Single exponential fits of the Langevin Dynamics signal traces in Figure 3.3, with temperature jumps as indicated.

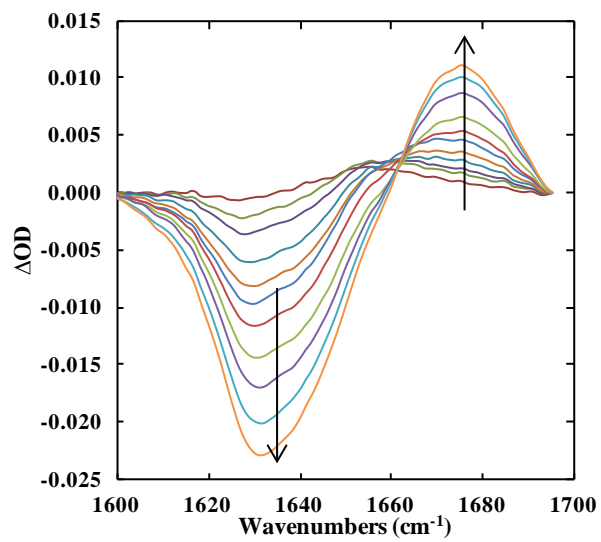


Figure 3.12. Difference FTIR spectra of BBL in the amide I' region, generated by subtracting the FTIR spectrum at 6.9 °C from those measured at higher temperatures (the highest temperature was 62.9 °C).

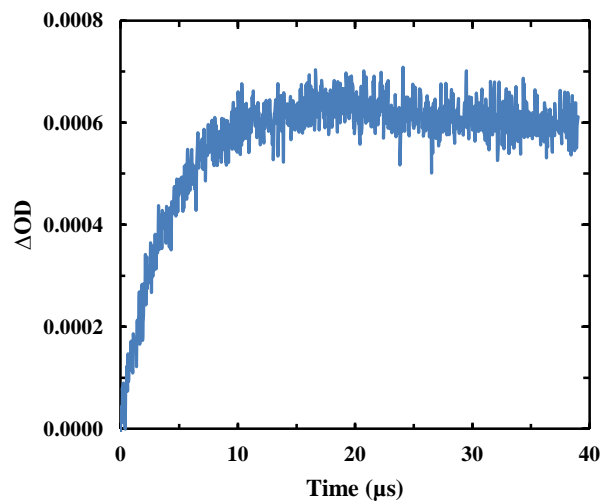


Figure 3.13. Conformational relaxation kinetics of BBL obtained with a probing frequency of 1668 cm^{-1} after a T -jump from 49.2 to $50.7\text{ }^{\circ}\text{C}$.

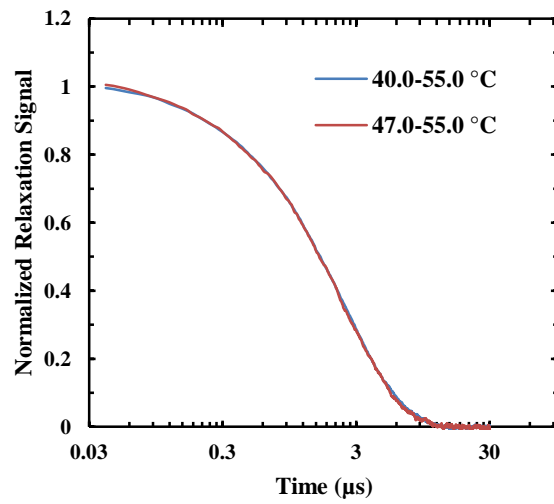


Figure 3.14. Simulated relaxation kinetics in response to T -jumps from different initial temperatures to the same final temperature, as indicated, for an incipient downhill folding scenario.

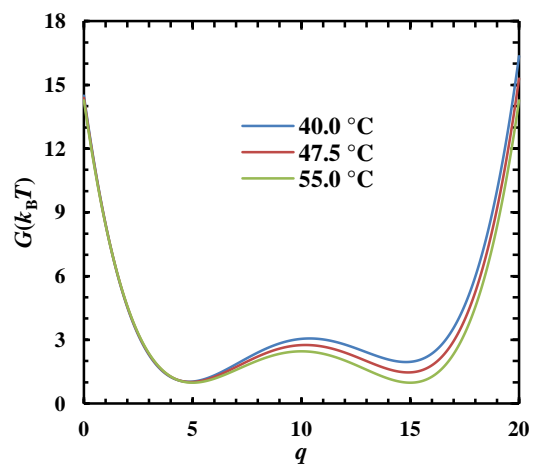


Figure 3.15. Free energy surfaces for an incipient downhill folding scenario used to simulate relaxation kinetics in Figure 3.14.

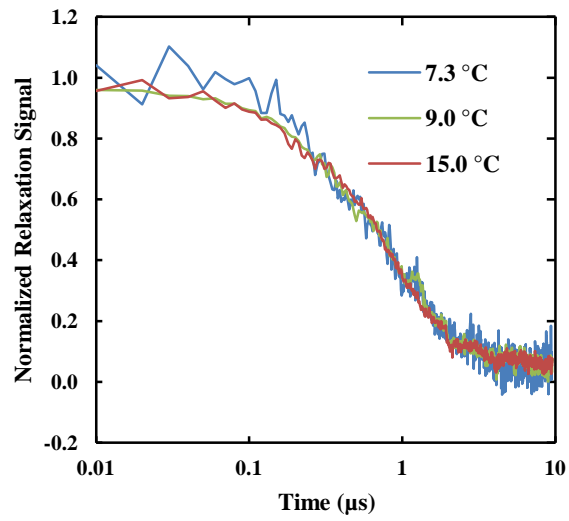


Figure 3.16. Relaxation kinetics of Trpzip-2c with different magnitude T -jumps, as indicated, to similar final temperature.

Name	Sequence
BBL	ALSPAIRLLAEHNLDASAIKGTGVGGRLTREDVEKHLAK-NH ₂
Trpzip-2c	AWAWENGKWAWK-NH ₂

Table 3.1. Name and sequence of the peptides studied.

	Temperature (K)	[F]%	[I]%	[U]%
A	298.0	80.55	17.97	1.48
	310.5	70.33	20.15	9.52
	323.0	42.24	15.54	42.23
B	298.0	80.55	17.97	1.48
	310.5	70.33	20.15	9.52
	323.0	42.24	15.54	42.23

Table 3.2. The equilibrium population percentage of each state (F: folded state, I: intermediate state, and U: unfolded state) corresponding to the free energies in Figure 3.2.

Mechanism	<i>T</i> -jump		Relaxation parameters of the folded state			
	T_i (K)	T_f (K)	τ_1 (μ s)	τ_2 (μ s)	A ₁ %	A ₂ %
A	310.5	323.0	1.85	33.96	8.87	91.13
	298.0	323.0	1.85	33.96	16.10	83.90
B	310.5	323.0	34.28	-	-	-
	298.0	323.0	34.28	-	-	-
Mechanism	<i>T</i> -jump		Relaxation parameters of the intermediate state			
	T_i (K)	T_f (K)	τ_1 (μ s)	τ_2 (μ s)	A ₁ %	A ₂ %
A	310.5	323.0	1.85	33.96	27.21	72.79
	298.0	323.0	1.85	33.96	42.42	57.58
B	310.5	323.0	1.85	33.96	63.07	36.93
	298.0	323.0	1.85	33.96	56.08	43.92
Mechanism	<i>T</i> -jump		Relaxation parameters of the unfolded state			
	T_i (K)	T_f (K)	τ_1 (μ s)	τ_2 (μ s)	A ₁ %	A ₂ %
A	310.5	323.0	34.03	-	-	-
	298.0	323.0	34.03	-	-	-
B	310.5	323.0	1.846	33.96	30.78	69.22
	298.0	323.0	1.846	33.96	24.95	75.05

Table 3.3. *T*-jump relaxation kinetic parameters calculated for the two three-state folding sensors presented in Figure 3.2.

Probe Frequency (cm ⁻¹)	T_f	T_i	$T_f - T_i$	τ_R (μ s)	Rel. Amp.
1668	46.8	38.1	8.7	3.3 ± 0.24	1.45
		41.1	5.7	4.5 ± 0.04	1.00
	50.7	44.4	6.3	2.6 ± 0.05	3.39
		46.5	4.2	3.0 ± 0.13	2.22
		49.2	1.5	3.4 ± 0.02	1.00
	57.0	44.4	12.6	2.0 ± 0.18	2.05
		53.3	3.7	2.8 ± 0.01	1.00
1630	46.5	39.2	7.3	3.4 ± 0.27	2.16
		43.6	2.9	4.9 ± 0.13	1.00

Table 3.4. Relaxation times of BBL obtained from fitting the corresponding T -jump IR relaxation kinetics to a single-exponential function.

Probing Frequency (cm ⁻¹)	T_f	T_i	$T_f - T_i$	τ_R (μ s)	Rel. Amp.
1630	61.8	46.8	15.0	0.90 ± 0.03	1.56
		52.9	9.0	0.92 ± 0.06	1.00
	72.4	52.5	19.9	0.50 ± 0.10	-
	57.8	41.1	16.7	1.10 ± 0.14	-

Table 3.5. Relaxation times of Trpzip-2c obtained from fitting the corresponding T -jump IR relaxation kinetics to a single-exponential function.

CHAPTER 4

Extracting the α -Helix Nucleation and Propagation Rates from the VIPT-Jump

Kinetics of an Alanine-Based Peptide

This chapter is recently prepared in manuscript and submitted to The Journal of Physical Chemistry.

4.1 Abstract

An infrared temperature-jump (T -jump) study by Huang *et al.* (*Proc. Natl. Acad. Sci.* 2002 99, 2788–2793) showed that the conformational relaxation kinetics of an alanine-based α -helical peptide depend not only on the final temperature (T_f) but also on the initial temperature (T_i) when T_f is fixed. This finding indicates that the folding free energy landscape of this peptide is non-two-state like, allowing conformational ensembles with different helical length and relaxation time to populate in the temperature range of the experiment. Because the α -helix folding involves two fundamental events, nucleation and propagation, the results of Huang *et al.* thus present a unique opportunity to determine their rate constants – a long-sought goal in the study of the helix-coil transition dynamics. Herein, we capitalize on this notion and develop a coarse-grained kinetic model to globally fit the thermal unfolding curve and T -jump kinetic traces of this peptide. Using this strategy, we are able to explicitly determine the microscopic rate constants of kinetic steps encountered in the nucleation and propagation processes. Our results reveal that the time taken to form an α -helical nucleus (i.e., an α -helical segment with one helical hydrogen bond) is about 320 ns, whereas the time taken to elongate this nucleus by one residue (or backbone unit) is 4.9 ns, depending on the position of this residue.

4.2 Introduction

The α -helix is not only ubiquitously found in proteins as a secondary structural element, it is also the folded conformation of many peptides. In this regard, the folding dynamics and mechanism of the α -helix have been extensively studied, either in the context of globular protein folding or as an individual and independent folding unit.^{27-28, 51, 54-55, 83-92} Currently, the most widely accepted theoretical framework to describe the α -helix folding properties is the helix-coil transition theory introduced by Zimm and Bragg⁹³ as well as Lifson and Roig.⁹⁴ In essence, this theory is a coarse-grained, one-dimensional (1D) Ising model, which treats the peptide in question as a linear chain of basic units, corresponding to the constituent residues or peptide groups that can adopt either a helical (H) or coil (C) state. Thermodynamically, a C to H (C \rightarrow H) transition leads to a decrease in the configurational entropy (ΔS) of the system, whereas the formation of a helical hydrogen bond (hH-bond) between two peptide groups that are in the H state (i.e., one at position i and the other at $i+3$) results in a favorable enthalpic gain (ΔH). Thus, based on the 1D Ising model,^{29, 31, 95} the free energy change (ΔG) upon formation of a particular helical conformation consisting of m hH-bonds and n H sites is: $\Delta G = m \cdot \Delta H - n \cdot T\Delta S$. Furthermore, the kinetics of the α -helix formation is described by a series of sequential events, wherein the consecutive C \rightarrow H transitions required to form the first hH-bond are regarded as the nucleation event, whereas the subsequent kinetic steps leading to lengthening of this nascent α -helical motif are referred to as the propagation process.

While such Ising-based models provide a sound theoretical framework for understanding the mechanism of the helix-coil transition,^{29, 95-99} it has proven rather difficult to experimentally assess the mechanistic details they infer, especially the microscopic rate constants of the nucleation and propagation events. This is due, at least in part, to the fact that (1) both events occur on a rapid timescale (i.e., on the nanosecond timescale for alanine-based α -helices);⁵¹ (2) their rates are not well separated;⁵⁷ (3) among the sequential kinetic events involved in α -helix folding, the first one (i.e., nucleation) is the slowest; and (4) there is not a simple experimental signal that can be used to distinguish nucleation from propagation. For example, although previous studies^{27-28, 90, 100} on various α -helical peptides were able to directly characterize the overall relaxation kinetics of the helix-coil transition in question, induced by either a rapid temperature-jump (T -jump) or a photo-isomerization event, they were unable to unambiguously separate and hence determine the respective contributions from the nucleation and propagation processes to the observed kinetic signals. In light of this difficulty, several recent studies have explored the possibility of isolating and therefore exclusively detecting a specific microscopic event in α -helix folding. These include (1) using short peptides that can form only a single turn of α -helix to assess the nucleation time via T -jump experiments,⁸¹ (2) using a photo-responsive cross-linker that induces a kink in an α -helix to probe the speed limit of the propagation process via transient two dimensional infrared (2D IR) measurements,¹⁰¹ and (3) employing a triplet-triplet energy transfer pair to assess local folding-unfolding dynamics of an α -helical peptide and using the resultant information to evaluate the helical propagation rate by analyzing the corresponding experimental results with the a kinetic Ising model.⁸⁰ Herein, we

demonstrate a new approach, which shows that the nucleation and propagation rates of an α -helix can be directly extracted by globally fitting its circular dichroism (CD) thermal unfolding curve and two T -jump kinetic traces, measured at the same final temperature but different initial temperatures, to a 1D Ising model.

A study by Huang *et al.*⁵⁷ showed that the conformational relaxation kinetics of an alanine-based α -helical peptide (referred to hereafter as AK peptide), in response to a rapid T -jump and as measured by time-resolved infrared (IR) spectroscopy, depend not only on the final temperature (T_f), as expected, but also on the initial temperature (T_i) for a fixed T_f (Figure 4.1). Since varying the initial temperature of the system in question is equivalent to varying its initial potential (VIP), we therefore refer to this type of T -jump kinetics as VIPT-jump kinetics. Our previous study⁴⁰ has shown that for a conformational relaxation process involving more than two conformational ensembles, its kinetics show a T_i -dependence for a given T_f . Therefore, the T -jump results of Huang *et al.* are not only consistent with the notion that the helix-coil transition kinetics involve multiple microscopic steps (e.g., nucleation and propagation) but also provide an additional piece of information that could be used to better determine their respective rate constants. This is because, as shown (Figure 4.2), the VIPT-jump kinetics of Huang *et al.* can be qualitatively understood in terms of three population ensembles (ES_1 , ES_2 and ES_3) having different helical conformational distributions and, in addition, going from ES_1 to ES_2 results in mostly shortening of the α -helices (and hence is fast), whereas converting ES_2 to ES_3 leads to a larger percentage of the α -helices to completely unfold (and hence, on average, is slower). Herein, we aim to capitalize on this picture and to extract the α -

helical nucleation and propagation rate constants by computationally fitting the VIPT-jump kinetics of Huang *et al.* to a 1D Ising-like model.

4.3 Results and Discussion

To determine the helical nucleation and propagation rate constants of the AK peptide, we use a kinetic 1D-Ising model to simultaneously fit its CD thermal unfolding curve and VIPT-jump kinetics. Our coarse-grained model treats each amide bond of the α -helix in question as a basic unit, which can adopt either a H or D state. As shown (Scheme 4.1), the AK peptide consists of 14 such units. This is because the D-Arg residue (i.e., **r**) and the SPE motif in its sequence were introduced to serve as helix caps, at the C- and N-terminus, respectively. In addition, since the experimental results of Huang *et al.* indicated that, as also observed for other α -helical peptides,^{39, 57, 80, 102} the middle region of the AK α -helix is more stable than its N- and C-terminal regions, we further divide those 14 units into three regions (referred to as the N-, C-, and M-region, respectively). Furthermore, we need to consider the fact that the VIPT-jump kinetics of Huang *et al.* were obtained by monitoring the amide' band arising from 4 ¹³C-isotopically labeled Ala residues in the middle of the AK peptide (Scheme 4.1) when computing the relaxation kinetics for comparison (see below).

Unlike what has been done in many previous studies,^{31, 95-96, 103} which often treated the folding thermodynamics and kinetics of the helix-coil transition in question separately, herein we seek to develop a sequential and fully reversible kinetic model to simultaneously characterize the thermodynamic and kinetic properties of the AK peptide.

The coarse-grained model of the AK peptide (Scheme 4.1) gives rise to a total of 2^{14} conformational states. Thus, without further approximation, one needs to consider $2^{14} \times (2^{14} - 1)$ elementary reaction steps in the calculation of its conformational relaxation kinetics, which is neither practical nor necessary. To reduce the number of rate equations, we assume that in one microscopic kinetic step only one amide unit is allowed to change its conformational state, either C→H (i.e., forward or folding reaction) or H→C (i.e., backward or unfolding reaction). While this assumption decreases the total number of kinetic equations to a more manageable one (i.e., 14×2^{14}), the corresponding kinetic analysis would still involve a large number of rate constants. Thus, we further make the following definitions and assumptions to reduce the number of variables or fitting parameters in the computer simulation: (1) the elementary steps leading to formation of a helical nucleus (i.e., ---CHHHC---) are considered as the nucleation events and have the same rate constant; (2) an elementary step leading to lengthening of a preexisting helical nucleus or helical segment is defined as a propagation step; (3) the nucleation rate constant (k_N) and the rate constant (k_{-N}) of the corresponding reverse reaction are position independent; (4) within an individual region (i.e., C-, M-, or N-region) the helical propagation rate constant (i.e., k_{PC} , k_{PM} , or k_{PN}) and the rate constant (i.e., k_{-PC} , k_{-PM} , or k_{-PN}) of the corresponding reverse reaction are position independent; and (5) only the unfolding rate constants are temperature dependent. Taken together, these assumptions reduce the total number of rate constants or variables in the model to 12.

Thermodynamic treatment. It is easy to show that once all of the microscopic rate constants of the system in question are known for a given temperature, one can easily compute the free energy of any helical state, relative to that (G_0) of the completely unfolded or disordered state (i.e., CCCCCCCCCCCCCC). As illustrated by a specific example (Scheme 4.2), when G_0 is set to be zero, the free energy (G_i) of any one of the possible conformational states can be evaluated (where i represents state i). Based on this information, the population weight (χ_i) of the i th state ($i = 0$ to 2^{14}) at the temperature (T) of interest can be further determined by

$$\chi_i(T) = \frac{\exp(-G_i/RT)}{\sum_i \exp(-G_i/RT)}, \quad (1)$$

where R is the gas constant.

Eq. (1) allows us to further evaluate the fractional helical content of the system at T , $\xi_H(T)$, which equals to the experimentally determined percent helicity at the same temperature via CD spectroscopy. It is straightforward to show that

$$\xi_H(T) = \frac{\sum_i N_i^H \cdot \chi_i(T)}{\sum_i N_{\max}^H \cdot \chi_i(T)}, \quad (2)$$

where N_i^H represents the total number of hH-bonds contained state i and $N_{\max}^H = 11$ is the maximum number of hH-bonds that the AK peptide can form.

In order to use Eq. (2) to fit the CD thermal unfolding curve of the AK peptide, we need to further convert the CD signal at T to $\xi_H(T)$. This is done by using the method of Baldwin and coworkers,¹⁰⁴ as shown below:

$$\xi_H(T) = \frac{[\theta]_{222} - [\theta]_C}{[\theta]_H - [\theta]_C} \quad (3)$$

with

$$[\theta]_H = -44000 \times \left(1 - \frac{2.5}{n}\right) + 100 \times T \quad (4)$$

and

$$[\theta]_C = 640 - 45 \times T \quad (5)$$

where $[\theta]_{222}$ is the mean residue ellipticity measured at 222 nm, $[\theta]_H$ is the mean residue ellipticity of the peptide with 100% helical content at 222 nm, $[\theta]_C$ is the mean residue ellipticity of the peptide with 0% helical content at 222 nm, and n is the number of residues of the α -helix.

Kinetic treatment. As indicated above, the VIPT-jump kinetics of Huang *et al.* were obtained by monitoring the amide I band of 4 ^{13}C -isotopically labeled Ala residues in the middle of the AK peptide. The amide I band is an established IR probe of protein secondary structures because of its dependence on interactions involving backbone amide groups, such as hydrogen bonding formation and transition dipole couplings.^{79, 82} Considering these factors, we assume that (1) only those amide units highlighted in gray in Scheme 4.1, all of which are able to form a hH-bond with one of the isotopically labeled amide units, can potentially contribute to the kinetics signal (S); (2) S is linearly proportional to the number of hH-bonds (N_{hHS}) formed within the signal region; and (3) $S = 0$ if there is only 1 hH-bond formed within the signal region (due to lack of vibrational coupling). For easy counting, we use the following equation in the computer program to determine N_{hHS} ,

$$N_{\text{hHS}} = \sum_{k=2}^8 \prod_{j=k}^{k+3} (P(j)), \quad (6)$$

where $P(j) = 1$ or 0 when the j th amide unit (within the signal region) is in the H or C state.

To fit the experimentally determined T -jump kinetic traces, the following master equation is solved numerically by a fourth-order Runge-Kutta algorithm,^{11, 40}

$$\frac{d}{dt}C(t) = \alpha^T \cdot r(t) \quad (7)$$

where C is the concentration vector, r is the rate vector, and α^T is the transpose of the stoichiometric matrix. Specifically, the C vector is a $2^{14} \times 1$ matrix, and the dimension of the α matrix is $14 \cdot 2^{14} \times 2^{14}$, where the rows correspond to the elementary reactions in the model and the columns represent the states of the peptide. The matrix elements in α correspond to the reactant and product coefficients of the corresponding elementary reactions. The rate vector, r , is a $14 \cdot 2^{14} \times 1$ matrix and contains all the rates of the corresponding elementary reactions in the model. To minimize the use of computer memory, the α matrix is further converted into a sparse matrix in the calculation. Since the commonly used single-sequence approximation^{29-30, 105} is not adopted in the current model, a single C→H (H→C) transition can lead to formation (breaking) of multiple hH-bonds due to the merging (splitting) of preexisting helical segments. For such conformational transitions, which are different from a simple propagation process, we evaluate their kinetics using a sequential model wherein the number of kinetic steps is determined based on the number of hH-bonds being formed (or broken).

Global fitting. During the global fitting of the two T -jump kinetic traces and the CD thermal unfolding curve of the AK peptide, only the aforementioned 12 elementary rate constants are treated as variables. In addition, we choose the lower initial temperature (i.e., 0.5 °C) and the final temperature (i.e., 14.5 °C) of the T -jump experiment of Huang

et al. as the two reference temperatures (T_1 and T_2). For a rate constant that is assumed to be temperature dependent, its values obtained at these two temperatures (i.e., k_{T1} and k_{T2}) are used to further calculate the corresponding free energy barrier, $\Delta G^\ddagger = \Delta H^\ddagger - T \cdot \Delta S^\ddagger$, via the following relationships:

$$\Delta H^\ddagger = -\frac{T_1 T_2 k_B}{(T_2 - T_1)} \cdot \left(\ln\left(\frac{k_{T1}}{A}\right) - \ln\left(\frac{k_{T2}}{A}\right) \right), \quad (8)$$

$$\Delta S^\ddagger = \frac{-k_B}{(T_2 - T_1)} \cdot \left(T_1 \cdot \ln\left(\frac{k_{T1}}{A}\right) - T_2 \cdot \ln\left(\frac{k_{T2}}{A}\right) \right), \quad (9)$$

where k_B is the Boltzmann constant and the value of A is set to be 10^{10} s^{-1} . With ΔG^\ddagger determined, the value of the rate constant in consideration at any other temperature T (k_T) can be further calculated via following equation:

$$k_T = A \cdot \exp\left(-\frac{\Delta G^\ddagger}{RT}\right). \quad (1)$$

Repeating this process for all other temperature-dependent rate constants would allow us to obtain all kinetic information required to determine the conformational distribution at T , hence allowing the CD signal at T to be evaluated.

Fitting results. As indicated (Figure 4.3), our coarse-grained kinetic model with 12 variables satisfactorily fits the CD thermal unfolding curve and the VIPT-jump kinetic traces of the AK peptide. It is worth noting that when these experimental data were individually fit to three equations, at least 16 variables would be required (i.e., 7 for fitting the CD curve to a two-state model and 4 for fitting each T -jump trace to a stretched exponential function). Therefore, in comparison we believe that the 12 rate constants recovered from the global fitting (Table 4.1) are statistically significant.

Perhaps more importantly, the fitting results are consistent with several expectations and previous studies. These include (1) for the nucleation process, the forward rate constant, $k_N = (103.9 \text{ ns})^{-1}$, is smaller than the backward rate constant, $k_{-N} = (23.0 \text{ ns})^{-1}$, which is consistent with the notion that the formation of an α -helix nucleus is a thermodynamically unfavorable event;^{29, 93, 106-108} (2) for the propagation process, the trend is reversed (for the temperature range considered), which consistent with the notion that propagation leads to α -helix stabilization;^{29, 39, 93, 108} (3) for the propagation process, the ratio between the forward rate constant and the backward rate constant is 3.1 for the M-region, 1.1 for the N-region, and 1.3 for the C-region, which is consistent with the fact that the middle region of an α -helix is more stable than its terminal regions;^{39, 57, 80} and (4) using the value of k_N , which, according to our model, is the rate constant of a single

C→H transition involved in the nucleation process, we determine the time required to form a helical nucleus (i.e., the ---CHHHC--- state in our model) to be about 318 ns. This value is in close agreement with that (i.e., 400 ns) reported by Kiefhaber and coworkers for an alanine-based peptide.⁸⁰ Similarly, using the propagation rate constant obtained for the M-region (i.e., k_{PM}), we calculate the time required to elongate a helical nucleus by 5 more hH-bonds (or 5 H sites according to our model) to be about 25 ns, which is again similar to that (50 ns) determined by Kiefhaber and coworkers.⁸⁰ Moreover, our results are also broadly consistent with the molecular dynamics (MD) simulation study of De Sancho and Best,³⁸ which showed that the timescales of the helix nucleation and elongation are 20-70 ns and ~1 ns, respectively, for an alanine-based peptide.

Finally, with the fitting results in hand, we can make a more detailed assessment of the helix-coil transition mechanism of the AK peptide. First, the conformational distribution calculated based on our model (Figure 4.4) indicates that there are a significant percentage of peptide molecules that contain more than one contiguous helical segment per peptide chain. This result argues against the applicability of the commonly used single-sequence approximation. Second, the free energy profiles obtained at 0.5 and 14.5 °C indicate that fully helical and disorder states are separated by a rather broad free energy barrier, located between 0 and 8 folded (or H) peptide units (Figure 4.5). Third, the minimum free energy surface is shallow at the folded side (Figure 4.5), allowing helical conformations with different helical chain length to populate. In addition, upon increasing the temperature from 0.5 to 14.5 °C, the helical conformation corresponding to the global free energy minimum is shortened from 11 H units to 8. A closer examination of the calculated conformational distribution at 14.5 °C reveals that most H units are

concentrated in the middle region of the peptide, a picture consistent with the fact that the helical structure in the terminal regions of an α -helix is less stable and tends to be frayed. As shown (Figure 4.6), the conformational distributions obtained at 0.5, 10.1 and 14.5 °C corroborate this notion as they indicate that, in this temperature range, increasing temperature does not lead to a simple population exchange, from the fully folded to the fully disordered conformation, instead it mostly results in a decrease in the average helical chain length. It is this (gradual) conformational shift, a scenario that is in agreement with our qualitative interpretation of the experimental observation of Huang *et al.* (Figure 4.2), that causes the T_i -dependence in the T -jump measurements and therefore is the key to allow the propagation kinetics detectable. In support of this notion, comparing the equilibrium conformation distributions determined for 0.5 and 14.5 °C of the peptide with the transient conformational distribution obtained at 200 ns of the conformational relaxation kinetics, induced by a T -jump from 0.5 to 14.5 °C, indicates that a conformational shift involving mostly propagation steps occurs early, whereas a global unfolding process involving the nucleation step takes place at a later time.

4.4 Conclusion

For a protein or peptide that can only sample a folded and an unfolded state, the single-exponential rate constant of its T -jump induced conformational relaxation kinetics only depends on the final temperature (T_f).⁴⁰ Thus, the study of Huang *et al.*,⁵⁷ which showed that the conformational relaxation kinetics of an alanine-based α -helical peptide exhibit a measurable dependence on the initial temperature (T_i) when T_f is fixed, not only suggests that the α -helix folding does not follow a two-state mechanism but also provides additional experimental information that can be used to determine the underlying nucleation and propagation rate constants. Taking advantage of this point, herein we develop a one-dimensional (1D) kinetic Ising model that involves 2^{14} conformational states and 12 fundamental rate constants to describe the folding kinetics and thermodynamics of this peptide. Using this model, we are able to globally fit the thermal unfolding curve and T -jump kinetics obtained by Huang *et al.*, and hence extracting the rate constants for the elementary kinetic steps involved in the helical nucleation and propagation processes. Our results show that for this alanine-based peptide the nucleation process (i.e., forming the first α -helical turn) takes places on a timescale of about 320 ns, whereas the process of lengthening a preexisting helical segment by one more unit (i.e., propagation) occurs as quickly as 5 ns.

4.5 Computational Methods

All calculations were carried out using specially written MATLAB programs (Mathworks, Natick, MA) on a Dell PowerEdge T610 computer equipped with two six-core Intel Xeon X5690 processors. Specifically, the differential equations were numerically solved by the fourth-order Runge-Kutta algorithm where the stoichiometric matrix was converted to a sparse matrix to reduce the usage of computer memory. Global fitting of the *T*-jump kinetics and the CD thermal unfolding curve of the AK peptide was done using the derivative-free pattern search algorithm¹⁰⁹⁻¹¹⁰ wherein the quality of the fitting was judged by the χ^2 value.

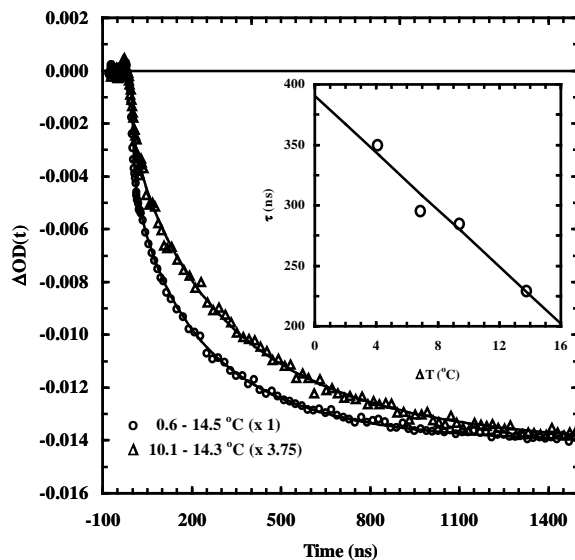


Figure 4.1. Normalized IR T -jump relaxation kinetics of the AK peptide, showing the dependence on T_i . Reprinted with permission from Reference 62 (Huang, C.-Y.; Getahun, Z.; Zhu, Y.; Klemke, J. W.; DeGrado, W. F.; Gai, F. Proc. Natl. Acad. Sci. U.S.A. 2002, 99, 2788-2793). Copyright 2002, Proceedings of the National Academy Sciences.

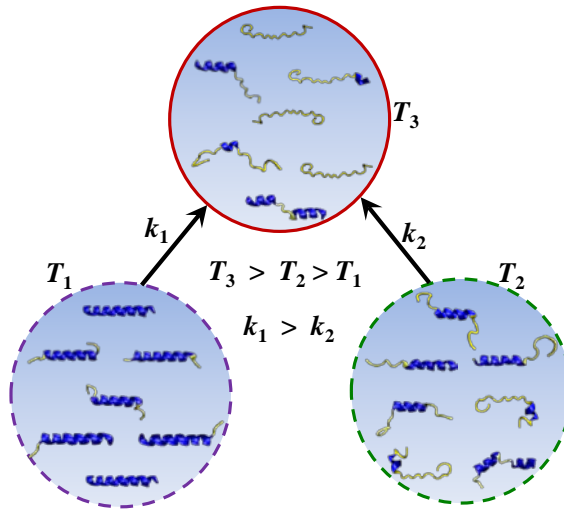


Figure 4.2. Cartoon illustration of the origin of T_1 -dependent conformational relaxation kinetics of an α -helix system.

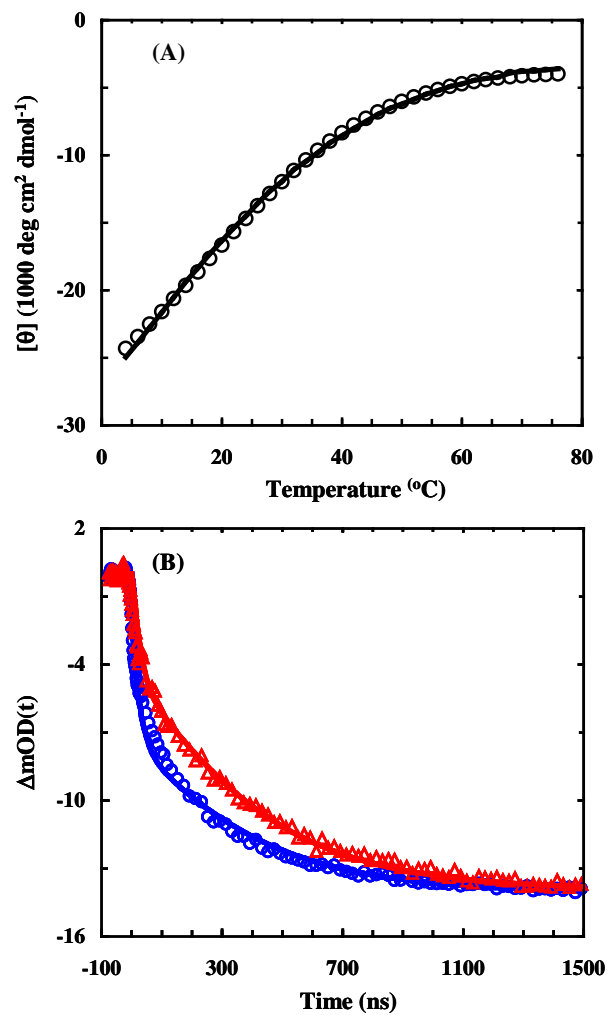


Figure 4.3. Global fitting results of the CD thermal unfolding curve (A) and the IR T -jump relaxation kinetics (B) of the AK peptide. In each case, the symbols represent the original experimental data and the line corresponds to the respective fit.

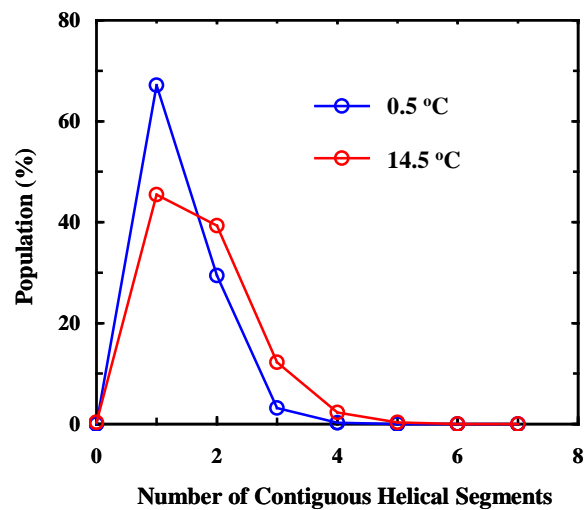


Figure 4.4. Conformational distribution of the AK peptide as a function of the number of contiguous helical segments per peptide chain at 0.5 and 14.5 °C, as indicated.

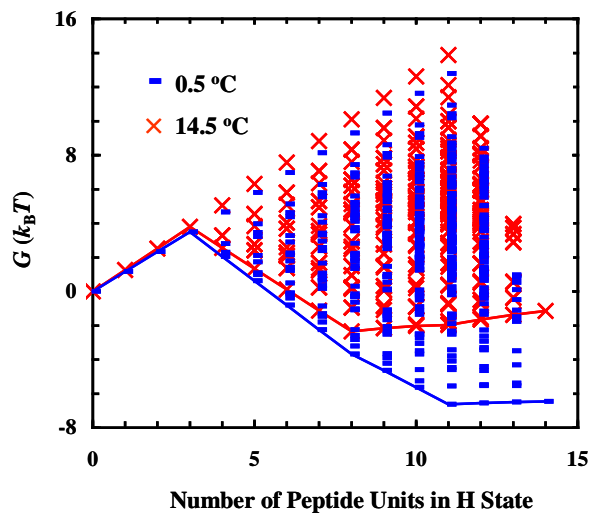


Figure 4.5. Free energy (G) of the AK peptide as a function of its conformation (i.e., the number of peptide units in H state) at 0.5 and 14.5 °C, as indicated. In each case, the line represents the minimum free energy surface.

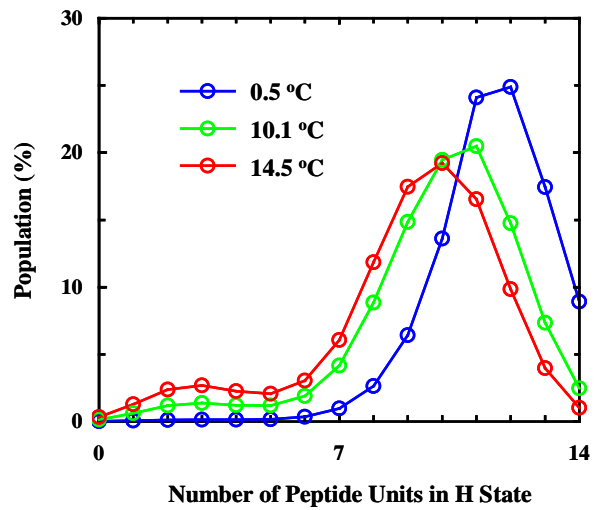


Figure 4.6. Conformational distribution of the AK peptide as a function of the number of peptide units in H state at 0.5, 10.1, and 14.5 °C, as indicated.

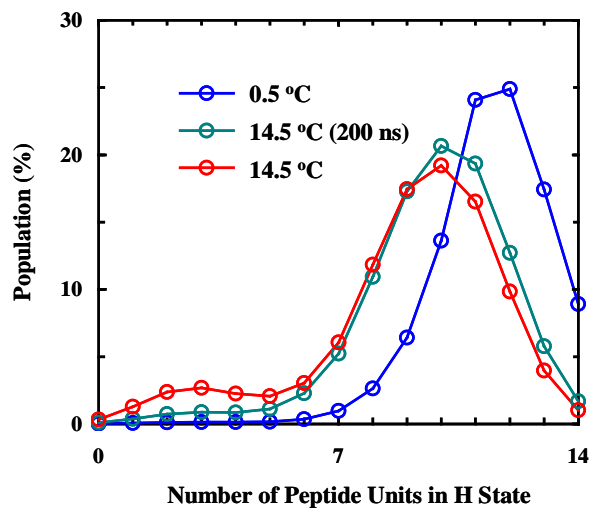
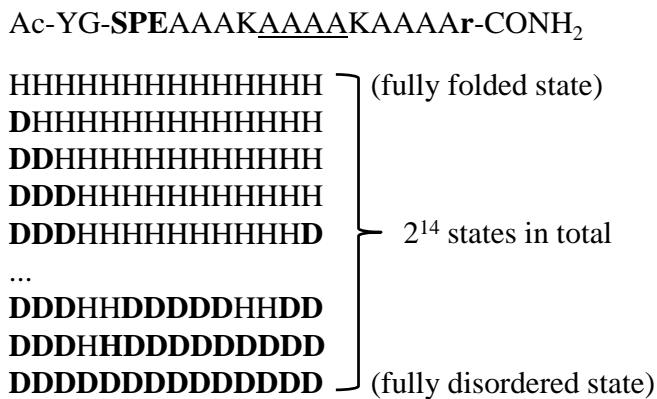
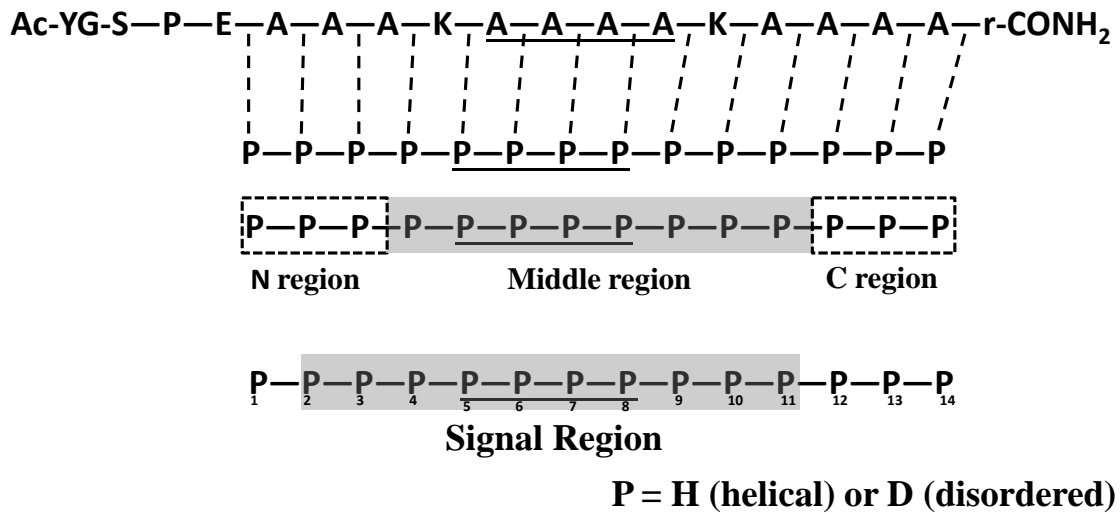


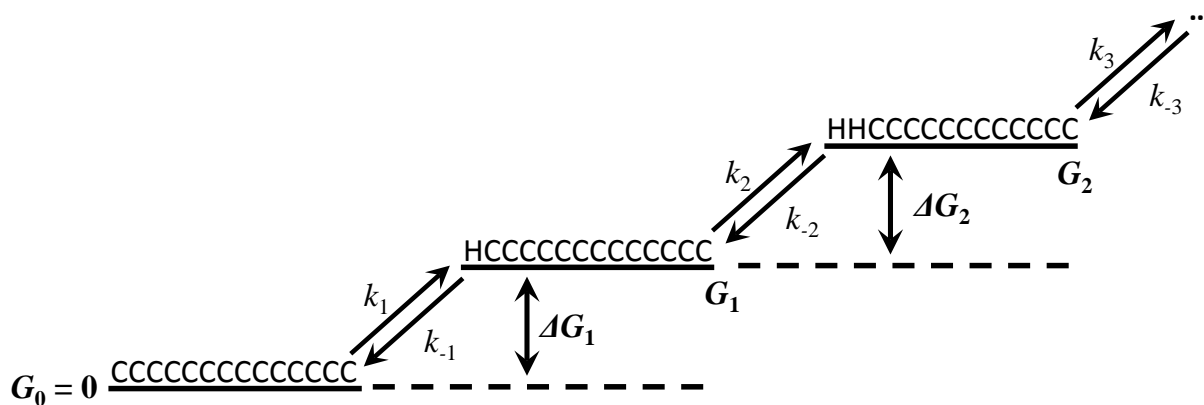
Figure 4.7. Comparison of equilibrium conformational distributions of the AK peptide at 0.5 and 14.5 °C with the transient conformational distribution obtained at 200 ns along the course of conformational relaxation induced by a *T*-jump from 0.5 to 14.5 °C.

	Folding (+)		$k_{+N} = (103.9 \text{ ns})^{-1}$		
Nucleation (N)		14.5°C	$k_{-N} = (23.0 \text{ ns})^{-1}$		
	Unfolding (-)	0.5°C	$k_{-N} = (28.3 \text{ ns})^{-1}$		
			N terminal region (N)	Middle region (M)	C terminal region (C)
	Folding (+)		$k_{+PN} = (12.0 \text{ ns})^{-1}$	$k_{+PM} = (4.9 \text{ ns})^{-1}$	$k_{+PC} = (91.7 \text{ ns})^{-1}$
Propagation (P)		14.5°C	$k_{-PN} = (13.2 \text{ ns})^{-1}$	$k_{-PM} = (15.2 \text{ ns})^{-1}$	$k_{-PC} = (116.6 \text{ ns})^{-1}$
	Unfolding (-)	0.5°C	$k_{-PN} = (17.6 \text{ ns})^{-1}$	$k_{-PM} = (16.5 \text{ ns})^{-1}$	$k_{-PC} = (206.4 \text{ ns})^{-1}$

Table 4.1. Rate constants obtained from the global fitting.



Scheme 4.1. The sequence of the peptide and few conformational states where "P" denotes the peptide group (or the amide unit), the basic unit of the coarse grained model in this study. For each P unit, it can only be in the helical (H) or coil (C) state. The string of P is the coarse grained 1D Ising model, which is aligned to the sequence of the peptide by the dash line indicating the corresponding position of the peptide for each coarse grained unit.



$$G_1 = G_0 + \Delta G_1 = 0 - k_B T \ln \left(\frac{k_1}{k_{-1}} \right)$$

$$G_2 = G_1 + \Delta G_2$$

Scheme 4.2. An example of how the free energy of the conformational state is defined where $k_1, k_{-1}, k_2, k_{-2}, k_3$ and k_{-3} are the rate constants for the elemental reaction which are selected from the elemental rate constant set.

CHAPTER 5

Measuring T -Jump Kinetics from Nanometer-Sized Water Droplets in Reverse Micelles

5.1 Abstract

Reverse micelles have become a useful system to study water molecules at the interfacial region and the protein loaded confined environment. In this study, we first combine an IR T -jump experiment with reverse micelles to extend the measuring time of the T -jump experiment. With the extended measuring time of the T -jump experiment, the gap in the measuring time range between the T -jump experiment and stop-flow experiment can be overcome. Both anionic and non-ionic surfactant are studied here to better understand the electrostatic interaction between the protein and the surfactant layer of the reverse micelles. The positively charged LysM is loaded into the non-ionic Igepal co-520 reverse micelle to study the folding dynamics. The conformational relaxation is determined to be 2.3 ms at 45.1 °C. Ubiquitin loaded into the negatively charged AOT reverse micelles reveals the unusual formation of aggregation. The LEA peptide is loaded into low w_0 reverse micelle to study the folding dynamics induced by dehydration, but limited information is obtained due to the low T -jump with the small sized reverse micelle.

5.2 Introduction

Over the past twenty years, the water pool confined in the nanoscopic reverse micelle has drawn much attention and been applied in many fields. By adding certain surfactants, water can be dissolved into oil, and the water pool is created through the microemulsion process which forms the self-assembled ternary system composed of oil, surfactant and water. The size of the water can be further controlled by the ratio of [water] to [surfactant]. The size-tunable water pool makes the reverse micelle an intriguing system for versatile applications. Since the size of the reverse micelle is on the nano scale, the ratio of the number of water molecules at the interfacial region between the water pool and the surrounding surfactant molecules is largely enhanced which provides a unique environment to study the solvent dynamics of water at the interface.¹¹¹⁻¹¹³ The confined aqueous environment can also work as a nano reactor to study the enzymatic reaction by encapsulating both the enzyme and the substrate into the reverse micelle.¹¹⁴ The confinement of the reverse micelle is also used in structural biology studies to force the folding of the protein and improve the structural resolution.¹¹⁵⁻¹¹⁷ In material science, comparing to regular micelles, reverse micelles can work as an alternative system to synthesize the nanomaterials and control their morphology. Duo to the similarity between the confined water pool of the reverse micelle and the water found in the biological system, which is usually in a crowd environment and closely interacts with proteins and membranes, reverse micelles act as a biological model system.¹¹⁸⁻¹¹⁹

In the conventional IR pump/IR probe *T*-jump experiment, a nanosecond IR pumping laser pulse is sent to heat up water in the sample within several nanoseconds with an increase of ~15 °C in temperature. The continuous-wave (CW) IR probing laser

is sent through the center of the pumping area to probe the optical density change caused by the incoming pumping laser pulse. Water is usually replaced by deuterium oxide (D_2O) to avoid the saturation in probing frequencies, since the strong absorption of the water vibrational bending mode at 1643 cm^{-1} is also the common region reported by the probes. Both D_2O and the conformational dynamics of the protein can contribute to the change in optical density ($\Delta O. D.$) at the probing frequency. The change contributed by D_2O can be subtracted by $\Delta O. D.$ of the reference cell with pure D_2O . After the subtraction, $\Delta O. D.$ is only contributed by the conformational dynamics of the protein which would reflect the conformational relaxation corresponding to the jump in temperature. The temperature dependence of optical density of water is further used as an internal thermometer by converting $\Delta O. D.$ of D_2O at the reference cell into the corresponding temperature change in T -jump experiment.

In the T -jump experiment, it is clear that the measurable time range for the measurement of the kinetic traces is limited by the heat dissipation from D_2O into the CaF_2 window and D_2O outside the pumping area. Therefore, the T -jump experiment is suitable for proteins which have a conformational relaxation timescale that is less than 1 ms. Usually, proteins with slower conformational relaxation times can be studied by the stopped-flow technique. However, the stopped-flow experiment has a dead time around 1 to 2 ms. A new method is needed to fill the gap of the measuring time range between the T -jump and the stopped-flow experiments. One way is to increase the time of heat retention in the sample to increase the measuring time range of T -jump experiment. Usually, aqueous solution is the common way for the sample preparation of the conventional T -jump experiment. However, here we use nonpolar organic solvent, which

has a smaller heat conductivity compared to water to slow down the heat dissipation process. The sample is made by the reverse micelle solution and the protein is further loaded in the nano water pool of the reverse micelle. By doing so, the T -jump experiment is now performed in the nano water pool. To our best knowledge, this is also the first study which uses the T -jump technique to study the folding dynamics of a protein in the reverse micelle.

5.3 Results and Discussion

The FTIR spectrum of AOT surfactant in isooctane shown in Figure 5.1 has relatively low optical density at the amide I' stretching region which makes AOT reverse micelles a good model system to study the protein folding dynamics using the amide I' stretching as the probe. In addition to the FTIR spectrum of the anionic surfactant, AOT, the FTIR spectra of nonionic surfactants of Brji30 and Igepal co-520 reverse micelles are shown in Figures 5.2 and 5.3. Likewise, they both have the absorption window to study the amide I' stretching mode of the protein. Due to the structural simplicity of the surfactant molecules studied here, they all have a relatively clean IR spectra. Therefore, they are not limited to probe only the amide I' stretching area. Other probes like azide and nitrile can also be used with these types of reverse micelles.¹²⁰⁻¹²⁵ By contrasting the results between the ionic and nonionic reverse micelle, the role of the surface charge in the confined nano water pool can be further interrogated. This will be discussed later with the protein in the reverse micelle. Figures 5.4 and 5.5 show the examples that LysM and LEA are loaded into the Igepal co-520 and AOT reverse micelles. The reverse micelles without protein in the reference cell allows the absorption spectra of the loaded protein to be extracted exclusively. After the basic investigation of the three reverse micelle surfactants and the protein in the reverse micelle from the steady-state IR spectroscopy, the following study is split into two parts. **1)** We first study the heat dissipation of from the nano D₂O pool into the bulk nonpolar organic solvent. The central idea is to use the low heat conduction nonpolar organic solvent as an insulator to keep the heat retained inside the nano D₂O pool. **2)** We study protein-folding dynamics in the reverse micelle to test the extended

measuring time range of the T -jump experiment and use the confined environment of the reverse micelle to study protein folding dynamics in the reverse micelle.

In part I, the normalized kinetic traces from bulk D_2O and the nano D_2O pool in AOT reverse micelles are shown in Figure 6. The kinetic traces probed at 1630 cm^{-1} are used to monitor the intensity change of the probing laser due to the OD change caused by T -jump. Because of the temperature dependence on the OD of D_2O , the kinetic trace reflects the temperature change of D_2O . For both traces, the temperature of D_2O is instantaneously increased by $\sim 10\text{ }^\circ\text{C}$ in a few ns and decays as the heat is released from D_2O into the nearby environment. There are two major differences in the heat dissipation process between the bulk pure D_2O and the nano D_2O pool. For the bulk pure D_2O , the heat can easily dissipate into the D_2O outside the pump area or into the contacted CaF_2 window. For the nano D_2O pool in the reverse micelle, the released heat has to cross the surrounding surfactant layer and diffuse into the nonpolar organic solvent. Both the nonpolar organic solvents, isooctane and cyclohexane, used in this study have a much smaller thermal conductivity when compared with water.¹²⁶ Therefore, better heat retention would be expected for the nano D_2O pool. It is clear in Figure 5.6 that the kinetic trace from the nano D_2O pool has a much slower process of the heat dissipation than that from the bulk D_2O . This shows that the low conductivity of the nonpolar organic solvent can improve the heat retention to extend the measuring time range of the T -jump experiment. To further improve the measuring time range of T -jump experiment, the mechanism of the heat dissipation from D_2O should be well investigated. In the future, a systematic study of reverse micelles with different w_0 can be used to understand the role of the surrounding surfactant layer on the effective contacting surface area between the

confined D₂O pool and the bulk nonpolar organic solvent by adjusting the ratio between the surfactant molecules and D₂O molecules. By comparing with different surfactant molecules in the reverse micelle system, the role of the surfactant molecular structure can also be clarified.

In part II, in order to test the extended measuring time range of the *T*-jump experiment and compare with the results from the stopped-flow experiment, LysM is loaded into AOT reverse micelle. However, the thermal stability of LysM is largely enhanced after being loaded into AOT reverse micelle. In Figure 5.7, the FTIR temperature dependence experiment of LysM in AOT reverse micelle shows the absorption of LysM in the amide I stretching region is relatively unchanged from 24.7 °C to 78.1 °C. This is possibly due to the electrostatic interaction between the positively charged LysM with multiple lysine residues and the negatively charged AOT surfactant anion. The electrostatic interaction may bring LysM to the negatively charged inner surface of AOT reverse micelle and further stabilize the structure of LysM which increases the difficulty of the folding dynamics measurement. Therefore, anion AOT surfactant is replaced by the nonionic Igepal co-520 surfactant. Figure 5.8 shows the conformational relaxation trace of LysM in Igepal co-520 reverse micelle after the *T*-jump from 40 to 45 °C. The trace probed at 1630 cm⁻¹ is fitted by a single exponential decay function with the fitted time constant of 2.3 ms which is similar to the value reported by the stopped-flow study. This result indicates the gap in the measuring time between the *T*-jump and the stopped-flow experiments can be filled by the combination of *T*-jump experiment with the reverse micelle. Furthermore, to study the stabilizing effect from the electrostatic interaction between the charged protein and surfactant

molecule, another protein, ubiquitin, which has the isoelectric point at 6.8, is loaded into AOT reverse micelle as the control experiment. Comparing to the isoelectric point of lysine side chain equal to 9.74, the net charge of ubiquitin should be around zero or slightly negatively charged which makes it a good control in the study of the electrostatic interaction with anionic AOT surfactant. However, the FTIR temperature dependence experiment from 24.7 °C to 78.0 °C in Figure 9 shows an increased peak at 1616 cm^{-1} as the temperature is increased, and the peak is not thermally reversible when the temperature goes back to 24.7 °C. This indicates an unusual phenomenon that ubiquitin confined in the reverse micelle aggregates especially since only one or two ubiquitin molecules at most are able to be loaded into the reverse micelle due to the size of the reverse micelle and the ratio between the reverse micelles and the ubiquitin molecules. Further studies on this unlikely aggregation may help us better understand the mechanism of protein aggregation which has become a thriving arena in protein science related to Alzheimer's disease, type II diabetes, etc.

Small w_0 reverse micelles are used as the model system to mimic the environment of dehydration and the protein folding dynamics related to the dehydrated environment can be studied by the combination of T -jump experiment with the reverse micelle. LEA peptide, which is an intrinsically disordered peptide that can be triggered to fold into a monomeric α -helix by removing the surrounding water, is loaded into AOT reverse micelle of $w_0 = 6$. Although LEA peptide is successfully loaded into the reverse micelle and the observable helical content is confirmed by CD, the T -jump measured from the nano D_2O pool is somehow limited under 4 °C. Such a small T -jump and the limited helicity would result in a relatively small amplitude of the conformational

relaxation traces in the T -jump experiment and increases the difficulty to extract the kinetic trace out of the background noise. Further effort is needed to improve the T -jump with the reverse micelle of low w_0 .

5.4 Conclusion

In this study, we combined an IR T -jump experiment with reverse micelles to slow down the heat dissipation from the nano water pool into the bulk nonpolar organic solvent. By comparing the kinetic trace from pure D_2O with the kinetic trace from the nano D_2O pool in the reverse micelle, it shows that the nonpolar organic solvent helps to retain the heat in the nano D_2O pool. This thus makes it possible to measure the folding dynamics from a slow folder, which is used to be measured by stopped-flow experiments, by a T -jump experiment. LysM is used to test the extended measuring time range of T -jump experiment with Igepal co-520 reverse micelle. The time constant of LysM conformational relaxation is determined to be 2.3 ms at 45 °C. Ubiquitin is loaded into AOT reverse micelle to study the electrostatic interaction between the loaded protein and the negatively charged AOT surfactant layer, and the unusual formation of aggregation may lead to a future study of the mechanism on protein aggregation. Moreover, AOT reverse micelles of low w_0 are used as the model system to provide the environment of dehydration to induce the folding of LEA peptide. However, the T -jump for the small size reverse micelle has to be improved before the further study of the folding dynamics in the reverse micelle of low w_0 .

5.5 Experimental Section

Peptide and Reverse Micelle Sample Preparation

LysM and Lea were synthesized by standard Fmoc (9-fluorenylme-thoxy-carbonyl) protocols using a PS3 automated peptide synthesizer (Protein Technologies, MA). Peptide products were further purified by reverse-phase high-performance liquid chromatography (HPLC) and identified by matrix-assisted laser desorption ionization time of flight (MALDI-TOF) mass spectroscopy. Trifluoroacetic acid (TFA) exchange was done by several rounds of hydrochloric acid solution additions and lyophilization. The purified peptide was lyophilized and stored in a -30 °C freezer. For IR measurements in D₂O solution, H-D exchange of the peptide was achieved by multiple rounds of mixing with D₂O and lyophilization. Ubiquitin was purchased from Sigma-Aldrich with no further purification and prepped with the same H-D exchange process.

Peptide and Reverse Micelle Sample Preparation

AOT surfactant was purchased from Fisher Scientific, Igepal co-520 was ordered from Rhodia, and Brji 30 is purchased from Acros Organics. All of them were used directly without any further purification. Nonpolar organic solvent, isooctane and cyclohexane, are both spectral grade solvent. The surfactant is first prepared in a stock solution of 0.5 M. The surfactant solution is further diluted by the nonpolar organic solvent and mixed with D₂O to the target concentration ratio between the surfactant and D₂O corresponding to the desired w_0 . The process of microemulsion is done by vortexing the mixture of surfactant solution and D₂O until the solution turns clear. To load protein

into the reverse micelle, D₂O is replaced by 20 mM phosphate D₂O buffer at pH 7. The protein is first dissolved by the buffer solution and then mixed with surfactant solution to have the protein solution encapsulated by the reverse micelle. D₂O at the reference cell is also replaced by buffer when the protein sample is studied.

Static and Time-Resolved Spectroscopic Measurements

Infrared spectra collected on a Magna-IR 860 spectrometer (Nicolet, WI) has 1 cm⁻¹ resolution. The sample cell is home made by CaF₂ windows with the optical path length of 55 μm.⁵⁷ For both types of measurement, protein in the reverse micelle solution had a bulk concentration of approximately 2.5 mM. A home-built laser-induced temperature jump (*T*-jump) apparatus is used to perform the time-resolved experiments. The detail of the setup is described elsewhere.^{27, 57, 127} For the *T*-jump kinetics reported, the probing frequency was in the region between 1668 and 1620 cm⁻¹, and the *T*-jump amplitude was about 5 – 12 °C.

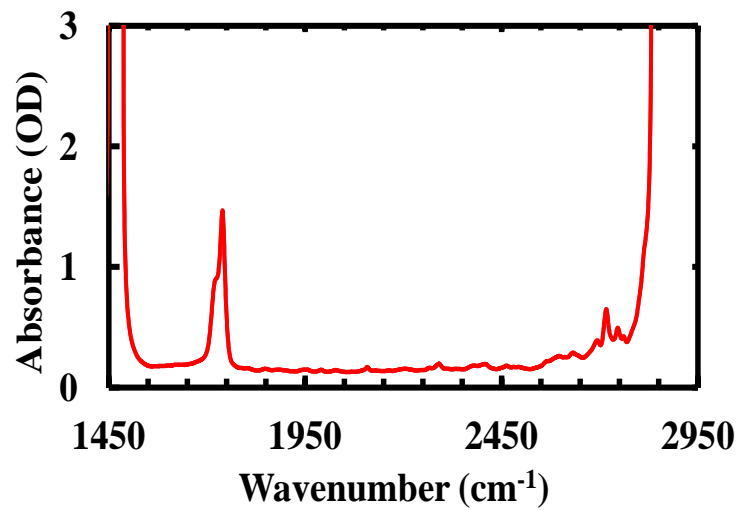


Figure 5.1. The Fourier transform infrared (FTIR) spectrum of AOT surfactant in isooctane

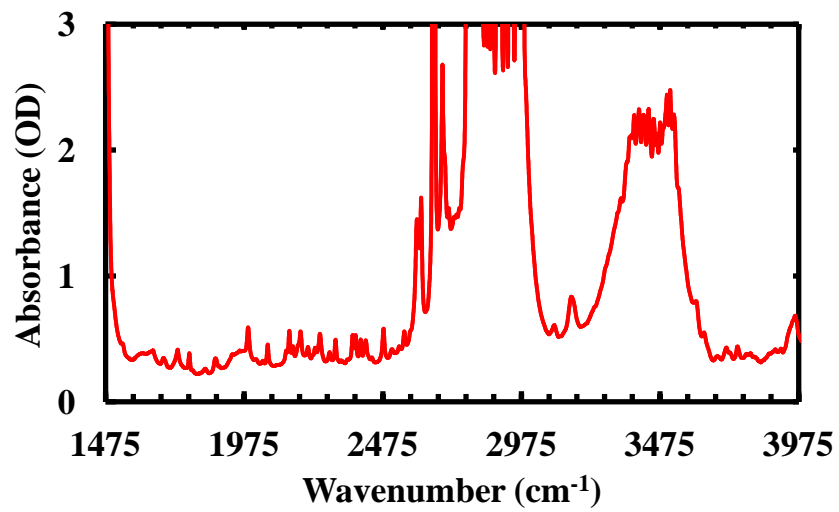


Figure 5.2. The FTIR spectrum of Brji30 surfactant in cyclohexane

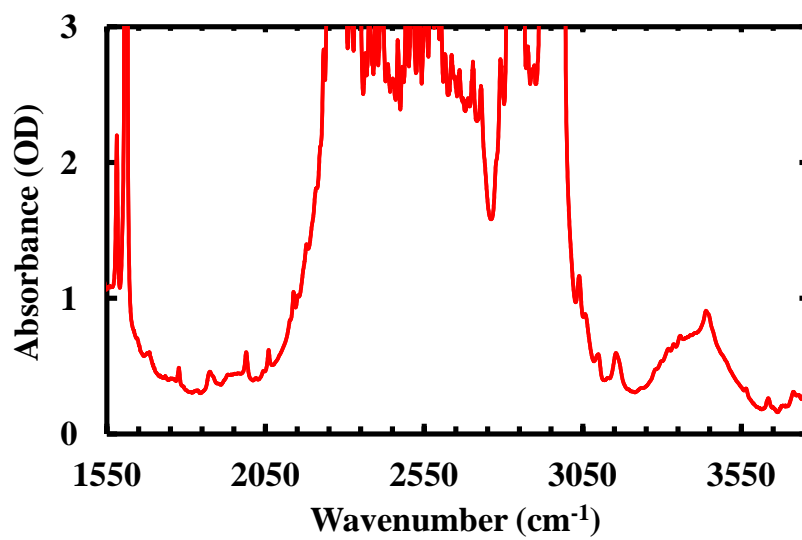


Figure 5.3. The FTIR spectrum of Igepal 520 reverse micelle with $w_0 = 30$

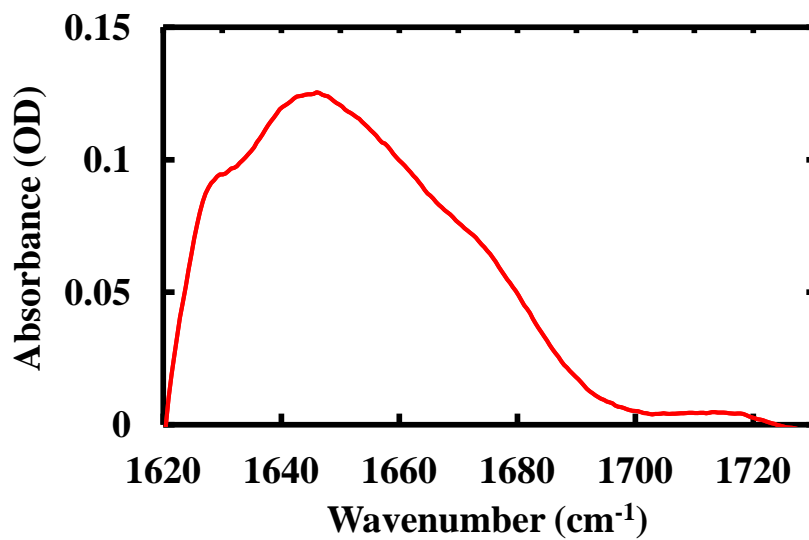


Figure 5.4. The FTIR spectrum of LysM in Igepal co-520 reverse micelle of $w_0 = 30$. The absorption from D2O and Igepal co-520 surfactant is subtracted from the reference compartment of the cell with only D2O in Igepal co-520 reverse micelle.

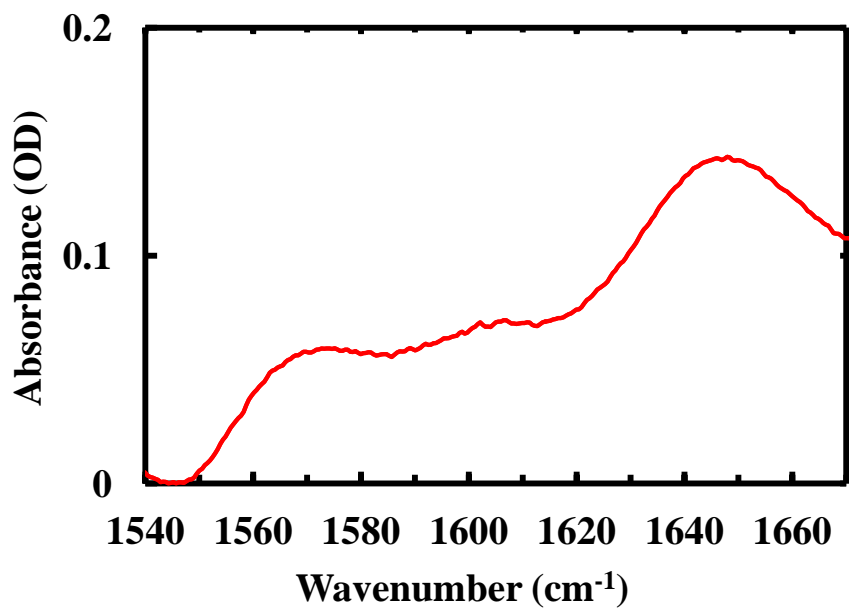


Figure 5.5. The FTIR spectrum of LEA peptide in AOT reverse micelle of $w_0 = 6$. The absorption contributed by D_2O and AOT surfactant is subtracted from the reference compartment of the cell with only D_2O in AOT reverse micelle.

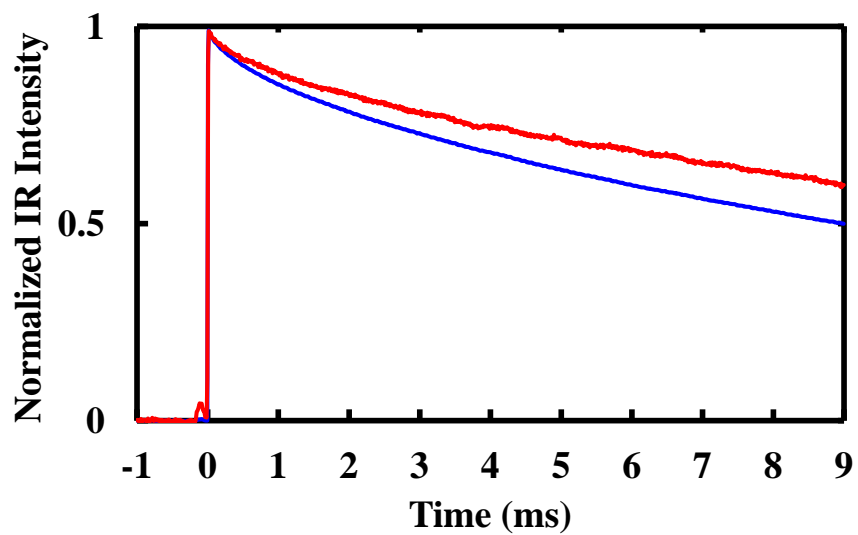


Figure 5.6. The normalized kinetic traces of the probing signal intensity at 1630 cm^{-1} caused by the change of the temperature in IR T -jump experiment. Red line is from D_2O in AOT reverse micelle of $w_0 = 30$ and blue is from bulk pure D_2O . Both traces are from different compartments of a FTIR cell.

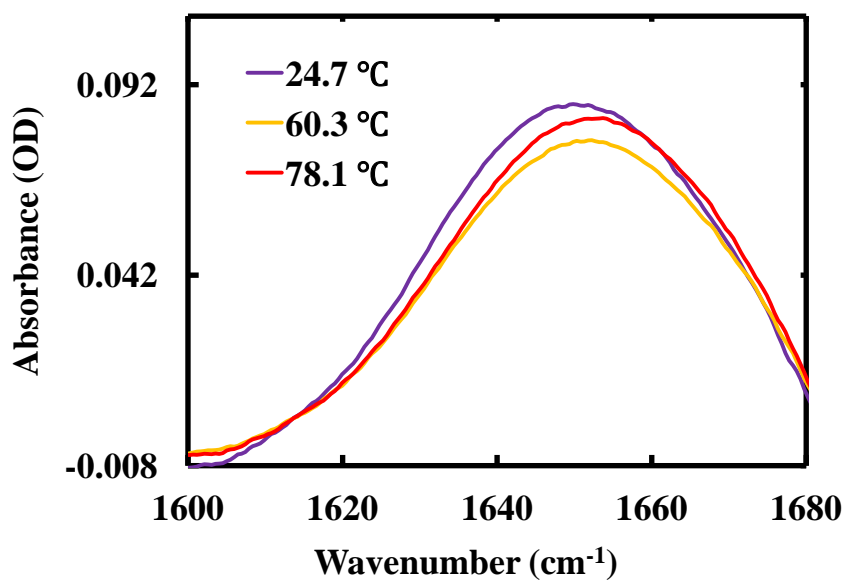


Figure 5.7. The FTIR temperature dependence experiment of LysM in AOT reverse micelle of $w_0 = 30$ at amide I' stretching region.

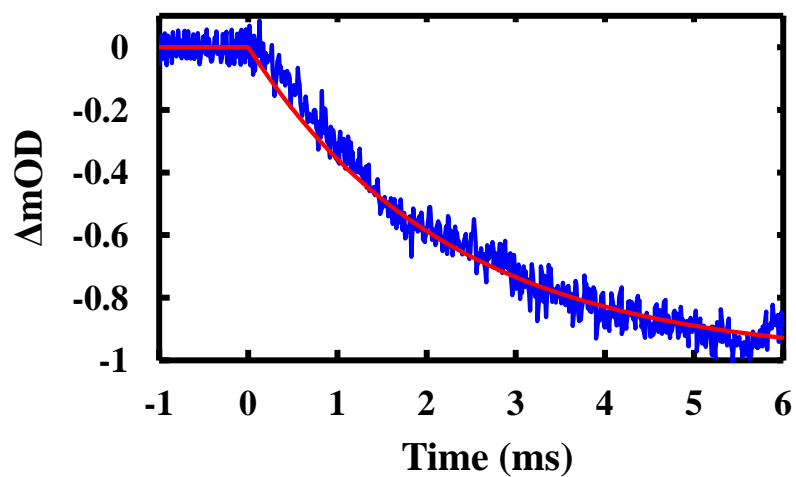


Figure 5.8. The kinetic trace of the conformational relaxation process from LysM in Igepal co-520 reverse micelle of $w_0 = 30$. The trace probed at 1630 cm^{-1} has a T-jump from $40.0\text{ }^\circ\text{C}$ to $45.1\text{ }^\circ\text{C}$. The red line is the single-exponential fitting curve with a time constant of 2.3 ms.

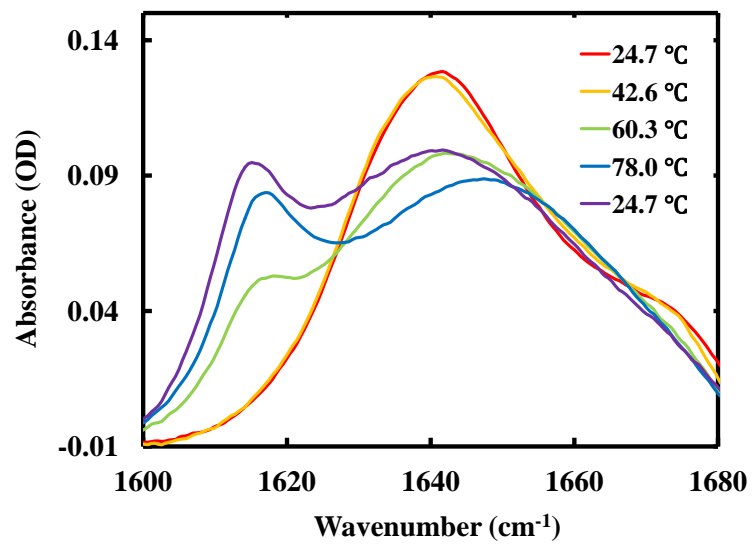


Figure 5.9. The FTIR temperature dependence experiment of ubiquitin at amide I stretching region.

CHAPTER 6

Conformational Dynamics of Influenza A M2 Proton Channel Probed by Photoinduced Electron Transfer Fluorescence-Quenching Correlation Spectroscopy

6.1 Abstract

Due to the threat of public health from the Influenza A virus, understanding the mechanism of how the virus invades the host cell becomes critical to developing the anti-influenza treatment. One strategy of the anti-influenza treatment is to block the function of the Influenza A M2 proton channel (AM2). One function of AM2 is to conduct protons from the endosome lumen to the virus envelope during the viral invasion. However, the mechanism of the proton conduction of AM2 is still unclear. Previous studies of AM2 have provided insight into the structure of AM2 in the closed form, the roles of the gating residues, His37 and Trp41, the possible binding sites of the anti-influenza A drugs, and the kinetics of proton conduction. However, dynamics studies of AM2, which are crucial to understanding the conduction mechanism, are rarely done. Here, we use photoinduced electron transfer fluorescence-quenching correlation spectroscopy (PET-FCS) to study the conformational dynamics of the AM2 transmembrane region. The time constant of the inter helix motion is first reported along with the transition between the closed and open states, providing new overall understanding of the proton conduction of AM2.

6.2 Introduction

The M2 protein of Influenza A virus consists of 97 residues and exists in the envelope of the virus as a homotetramer.¹²⁸ One important function of this M2 tetramer, which forms a pH-responsive channel, is to assist protons to unidirectionally across the viral membrane, allowing acidification of the viral interior in the endosome lumen.¹²⁸⁻¹²⁹ Because this acidification event plays a key role in viral replication, the M2 proton channel has become a popular anti-viral drug target.¹³⁰ As such, many studies have been devoted to elucidating its proton conduction and inhibition mechanisms.¹³¹⁻¹³⁵ In particular, significant progress has been made in recent years in structure-based studies,¹³⁶ providing much needed molecular insight into the understanding of the pH-activated, asymmetric proton conduction action of the M2 proton channel. While existing models¹³⁷⁻¹⁴⁴ differ in details with regard to the mechanism of proton conduction, they share several common features: (1) proton selection and channel activation are primarily controlled by His37 tetrad (Figure 1), (2) channel is activated or transitioned from a closed to an open state when three His37 residues are protonated at an acidic pH, (3) the role of Trp41 tetrad (Figure 1) is to allow unidirectional proton conduction only when the pH is low on the outside of the virus, and (4) channel waters are actively involved in proton conduction. Although we now know a great deal about the structure of this membrane-spanning channel and many thermodynamic aspects of its mechanism of action, we know relatively little about the underlying dynamics that control the rate of proton conduction. Herein, we aim to address this question by using a single-molecule fluorescence technique to assess the conformational dynamics of the M2 channel in model membranes.

As a necessary process for proton conduction, protonation-deprotonation of His37 could be the rate-limiting step.^{140, 144} However, the study of Hong and coworkers¹⁴⁵ found that the His37-water proton exchange rate ($\sim 10^5 \text{ s}^{-1}$) is significantly higher than the time-averaged unitary proton flux of M2, suggesting that additional steps need to be included in the kinetic mechanism in order to explain the observed rate of proton conduction. In fact, several scenarios have been proposed, including (1) the His37-Trp41 cation- π interaction can periodically form and breaks at low pH,¹⁴⁶ thus modulating the rate of proton conduction, (2) a recycling step is required after each proton release,¹⁴⁷ which involves closing the Trp41 gate and opening the Val27 gate and hence decrease the rate adds additional time for proton conduction, (3) even at low pH the C-terminal open conformation (i.e., the conformation that allows transfer of protons from His37 to the interior of the virus) is only transiently populated,¹⁴⁸ leading to a slower apparent rate, and (4) proton migration from water cluster B to C (Figure 1) requires an additional conformational transition that involve Trp41 via either sidechain or backbone motions.¹⁴⁹ Given that Trp41 is involved in all those scenarios, we carry out a single-molecule fluorescence experiment to directly assess its conformational dynamics under equilibrium but different pH conditions using both the full-length M2 protein and a truncated variant corresponding to the transmembrane domain of M2 (referred to as M2TM).

Our experimental design is based on the notion that Trp can effectively quench the fluorescence of oxazine dyes, such as Atto655.¹⁵⁰⁻¹⁵¹ Because this quenching effect arises from a photoinduced electron transfer (PET) process, it requires the quencher (Trp) to be sufficiently close to the fluorophore (dye). In addition, as the rate of PET is sensitively dependent on the quencher-fluorophore separation distance (R_{QF}), it is possible

to utilize a Trp-dye pair and fluorescence correlation spectroscopy (FCS) to characterize the rate of a specific protein conformational motion, as long as this motion modulates R_{QF} and hence induces fluctuations in the fluorescence intensity.¹⁵²⁻¹⁵⁴ To employ this PET-FCS strategy to assess the conformational dynamics of Trp41 in the full-length M2 and M2TM proton channels, we introduce an Atto655 dye at position 40 via a Cys residue using a double mutant of the respective native sequence, Leu40/Cys-Trp41/Phe (the labeled peptide and protein are hereafter referred to as M2TM* and M2*, respectively). The reason that we use a Trp41/Phe M2 (M2TM) mutant to carry the Atto655 fluorescence reporter is to eliminate the intra-molecular quenching effect arising from the Trp residue on the same helix in the tetramer, which, when present, would dominate the observed PET-FCS signal.¹⁵⁵ To use M2* (M2TM*) to report the motion of Trp41, we use a mixture of wild-type M2 (M2TM) and M2* (M2TM*) to prepare the corresponding membrane-bound tetramers. By specifically controlling the ratio between the labeled and non-labeled proteins (peptides), we ensure that the large majority of tetramers thus prepared contain either no or only one M2* or M2TM*. Because in a M2* (M2TM*) containing tetramer only inter-molecular quenching effect can occur, the PET-FCS signal thus provides a direct measurement of the underlying Trp41 dynamics. Our results show that Trp41 is subject to a conformational motion that occurs on a timescale of tens to hundreds of microseconds, depending on pH, membrane composition, and the identity of the proton channel (i.e., full-length M2 or M2TM). To the best of our knowledge, we believe that this is the first study revealing that the M2 proton channel undergoes a spontaneous conformational fluctuation on the microsecond timescale.

6.3 Results and Discussion

Since the He/Ne laser source of the FCS setup in this study is changed to be circularly polarized by a visible polarizer and a $\lambda/4$ waveplate (See Experimental Section), the fluorescence fluctuation of the anisotropic excitation from the rotation of LUV can be eliminated. Therefore, a conventional FCS model comprised of the diffusion part and dynamics part is used to describe the FCS traces (see below).

$$G(\tau) = \frac{1}{N} \cdot \left(\left(\frac{1}{1 + \frac{\tau}{\tau_D}} \right) \cdot \left(\frac{1}{1 + \frac{\tau}{\omega^2 \tau_D}} \right)^{1/2} \right) \times \left(\frac{1 - \sum_{i=1}^m \left(T_i - T_i \cdot \exp\left(-\frac{\tau}{\tau_i}\right) \right)}{1 - \sum_{i=1}^m T_i} \right) \quad (1)$$

where τ_D is the 3-D diffusion time constant, ω is the axial- to lateral-dimension ratio of the confocal volume, N is the number of fluorescent molecules in the confocal volume, and τ_i and T_i

are the respective time constant and amplitude of the dynamics component i . The value of ω was determined by the results of the fluorescent Atto 655 dye in water.

First, the FCS experiment is conducted at different pHs with LUVs made of POPC/POPG/Cholesterol (4/1/2) since cholesterol is reported to improve the stability of AM2 tetramer structure on the membrane. By fitting the model of Equation 1 to the FCS traces at different pHs with two diffusion components for LUV diffusion, one dynamics

term for triplet state population, and another one dynamics term for PET, the time constant of PET components can be extracted from τ_{PET} of PET. The reason to use two diffusion terms is to account for the size dispersion of the LUVs. The triplet population is due to intersystem crossing at the first singlet excited state (S_1) of the fluorescence dye and also results in the fluctuation in fluorescence. Therefore, a dynamics term has to be attributed to this. The fluorescence fluctuation due to the quenching process from PET is taken into account by another dynamics term. All the individual fitted curves and detailed fitted results are shown in the Appendix.

Figure 6.1 shows a representative example of the fitting for one M2TM FCS curve. It is clear that at pH = 5, M2TM has a strong fluorescence fluctuation due to the non-diffusive process, especially the curve corresponding to the pure diffusion of LUV (black dashed line). The time constants of PET at pH from 5 to 8 are summarized in Table 6.1. Since the ratio between Atto 655 labeled DMM2TM and WT M2TM is 0.04, there would be either one or none labeled helix in the four-helix bundle. Therefore, PET becomes an inter-helix event in the M2 proton channel. Furthermore, due to the relatively short-range interaction of PET usually through the collision between the electron donor and acceptor, PET is indeed sensitive to the motion within the channel (inter-helix motion). Figure 6.2 shows the dependence of the PET time constant on pH. The pH dependence clearly matches the titration curve of His37 from other studies where His37 is believed to work as the switch of the proton conduction in the M2 proton channel through a protonation and deprotonation mechanism. Therefore, the pH dependence of PET indicates the probed inter-helix motion synchronizes with the conductance of M2 proton channel. Indeed, the inter-helix motion can be treated as the global motion of the

M2 proton. To our best knowledge, this is first time that the conformational dynamics of M2 proton channel along with the open and close state is captured by the inter-helix motion.

To further interrogate the inter-helix motion of M2 proton channel, the effect of lipid composition on the inter-helix motion is studied. It was reported by Christian *et al.* that cholesterol in the lipid composition is critical to stabilize the four helices bundle structure of M2 proton channel.¹⁵⁶ By removing cholesterol from the lipid composition, the FCS measurements are repeated from pH 5 to 8 to see the corresponding change reflected by the inter-helix motion without the stabilizing effect. The pH dependence of PET time constant is observed again, and the data are summarized and plotted in Table 6.2 and Figure 6.3. Although the pH dependence of PET without cholesterol looks similar to the pH dependence of His37 (see Figure 6.3.), the difference between the dependence with and without cholesterol is clear when two sets of data are shown together in Figure 6.4. It shows that the data set from the lipid without cholesterol is shifted to the direction of lower PET time constant and higher pH which indicates that the inter-helix motion becomes faster and the conduction of proton is activated at higher pH. Many studies have shown that cholesterol can increase the fluidity of lipid membrane and help to maintain structure of cell membrane. The faster inter-helix motion is expected due to the absence of cholesterol in the lipid membrane. Furthermore, the proton conduction activation at higher pH implies that the closed form of M2 proton channel requiring higher structural stability to keep the channel closed is destabilized by the absence of cholesterol.¹⁵⁶

6.4 Conclusion

This study shows that PET-FCS can be used to study the conformational dynamics of the M2 proton channel. The time constant of PET is attributed to the dynamics of the inter-helix motion, and shows similar pH dependence as the titration curve of His37 in the M2 proton channel. Since His37 is believed to work as the gating unit of M2 proton channel via its protonation and deprotonation mechanism, the matched pH dependence of PET allows us to treat the inter-helix motion as the global motion corresponding to the conductance of the M2 proton channel. The inter-helix motion is further shown to be sensitive to both the structural stability of the four-helix bundle and the fluidity of the lipid membrane by using cholesterol in the lipid composition as the control. We believe this is the first time that the conformational dynamics from the inter-helix motion is reported. The conformational dynamics should be included by future dynamics simulation studies to better model the proton conduction of the M2 proton channel. Understanding the dynamics of the M2 proton channel is key to unveiling the mechanism of the proton conduction; for example, why the channel has such high selectivity for protons and how the rate of the proton conduction is maintained. Further PET studies on the dynamics of the M2 proton channel with different types of PET pairs or different locations of PET pairs for the global or local dynamics are indeed required.

6.5 Experimental Section

Peptide Synthesis and Purification.

Peptides were synthesized by the peptide synthesizer (PS3) using solid-phase Fmoc synthesis, and further cleaved and purified as previously described.¹⁵⁷ The sequence of WT M2TM peptide (22-46) is SSDPLVVAASIIGILHLILWILDRL. The M2TM –for Atto 655 dye labeling reaction has two mutations, L40C and W41F. This peptide is referred to as DMM2TM in this study. After the purification by reverse-phase high performance liquid chromatography (HPLC), peptides were lyophilized, and identified by matrix-assisted laser desorption ionization (MALDI) - time of flight (TOF) mass spectrometry.

Peptide Labeling.

The thiol side chain of Cys40 DMM2TM peptide were labeled with Atto 655 dye. Labeling reactions were performed with an 10-fold excess of dye to peptide. DMM2TM was weighed, and dissolved in phosphate buffer (pH = 7), and mixed with the corresponding amount of Atto 655 maleimide reactive dye (Sigma-Aldrich, St. Louis, MO) which is first dissolved in water. Total reaction mixture volumes were around 1.5 mL. The reaction mixture was stirred at room temperature for 2 h and left in a 4 °C fridge overnight. The reaction mixture was further purified by HPLC with a reverse-phase analytical C18 column with serial injections to remove the free reactive dyes. The elution gradient was similar to other studies with the preparative purification of M2TM.¹⁵⁸⁻¹⁵⁹ The blue colored labeled peptide was lyophilized and identified by MALDI-TOF mass

spectrometry. The yield of the labeled DMM2TM was further determined by dissolving the labeled peptide into water and using Atto 655 extinction coefficient of $125000 \text{ M}^{-1} \text{ cm}^{-1}$ at 680 nm.

M2TM Reconstitution into Large Unilamellar Vesicle (LUV)

The lipid chloroform stock solution is made by 2.5 μmol total lipid molecules of 4:1 POPC/POPG or 4:1:2 POPC/POPG/Cholesterol (Avanti Polar Lipids, Alabaster, AL) in chloroform. The stock solution was further mixed with WT M2TM (1.25 nmol, 1:2000 monomer/lipid) in 40 mM octylglucoside (OG) (<50 μl) and 0.05 nmol (1:50 000 monomer/lipid). Atto 655 labeled DMM2TM was dissolved in 2,2,2-Trifluoroethanol (TFE) (<10 μl) due to the limited solubility in aqueous solution. Next, the mixture was dried by a stream of nitrogen and left under the vacuum of the lyophilizer for more than 2 h. If the lipid film is not used immediately, the film would be stored at $-20 \text{ }^\circ\text{C}$. To make the LUV solution, the film was hydrated with 1.2 ml buffer solution of 50 mM phosphate and 100 mM NaCl for pH 6 - 8, and 50 mM sodium acetate and 100 mM NaCl for pH 5 - 6. After vortex mixing, the mixture underwent 8 freeze-thaw cycles and the extrusion of the solution was made by an extruder with a 100 nm pore-size membrane filter (Avanti Polar Lipids, Alabaster, AL).

FCS Sample Preparation.

Due to the free labeled peptides and OG in the LUV sample, the LUV solution was further purified by the PD-10 desalting column (GE Healthcare Bio-Sciences, Pittsburgh, PA) right before the use. The PD-10 was washed by ultra-pure water (EMD Millipore, Darmstadt, Germany) and pre-equilibrated with the same buffer solution of the LUV sample. The coverslips (Fisher Scientific) required additional steps for passivation before use. They were sonicated in 5% NaOH aqueous solution for 30 min. After being cleaned by ultra-pure water, the coverslips were soaked into the saturated casein (Fisher Scientific) solution overnight. The next day, the coverslips were rinsed by ultra-pure water and dried with compressed air before use. For regular FCS measurements, a 40 μ l M2TM LUV sample was loaded onto the specially passivated coverslips. The remaining passivated coverslips were stored in a dry box for future use.

FCS Setup and Measurement

The details of the FCS setup is described in our other studies.^{127, 160} In the current case, excitation of the Atto 655 dye was accomplished by the 30 mW 632 nm line of a Helium/Neon laser (JDS Uniphase Corporation, Milpitas, CA). The polarization of the laser line was made circular by one high quality visible polarizer (Thorlab Inc., Newton, NJ) and a zero order $\lambda/4$ quartz waveplate (Edmund Optics, Barrington, NJ) in this study to avoid the anisotropic excitation of the labeled peptide due to LUV rotation. Moreover, each 1.1 ml M2 LUV sample after extrusion was split into two 0.55 ml samples for

further purification by a PD-10 desalting column. The PD-10 desalting column purified sample was immediately loaded onto the coverslip of the FCS setup, and only two FCS curves were accumulated for one purified M2 sample with the duration of 300 s to avoid the signal contributed from the free labeled peptide released from LUV. An average of 4 such FCS curves at each pH was used in the subsequent data analysis.

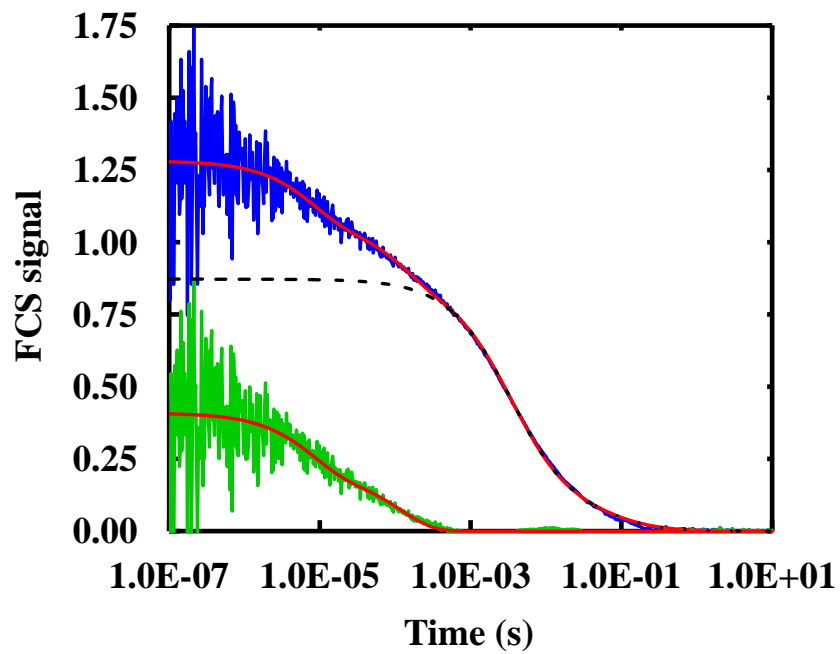


Figure 6.1. The fitting of FCS curve from M2TM at pH = 5 where blue line is the overall observable FCS trace, dashed black line is the fitted diffusion component of LUV, green is the overall dynamics subtracted by LUV diffusion, and the red lines are the fitting curves.

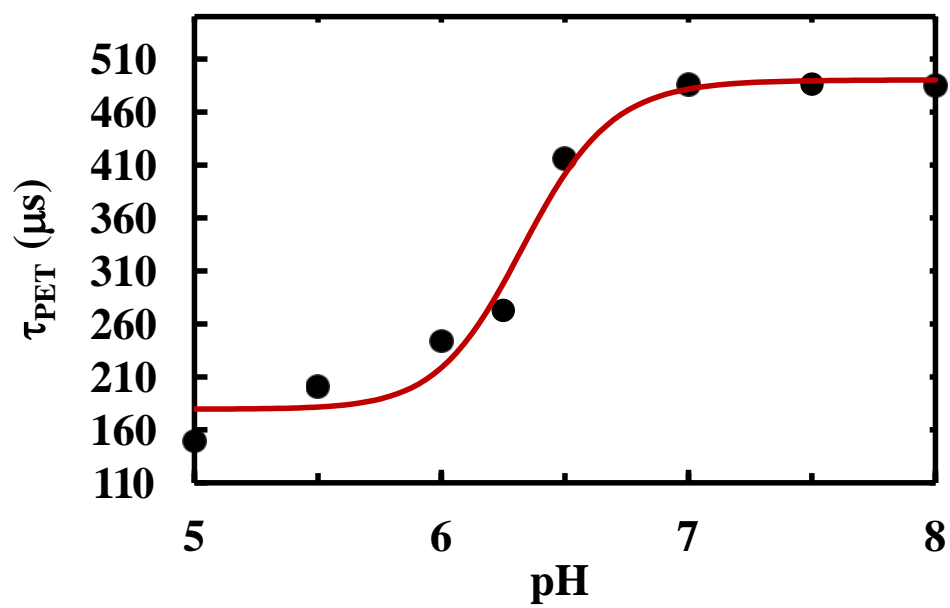


Figure 6.2. The plot of PET time constant to pH of M2TM with the lipid composition of POPC/POPG/Cholesterol (4/1/2)

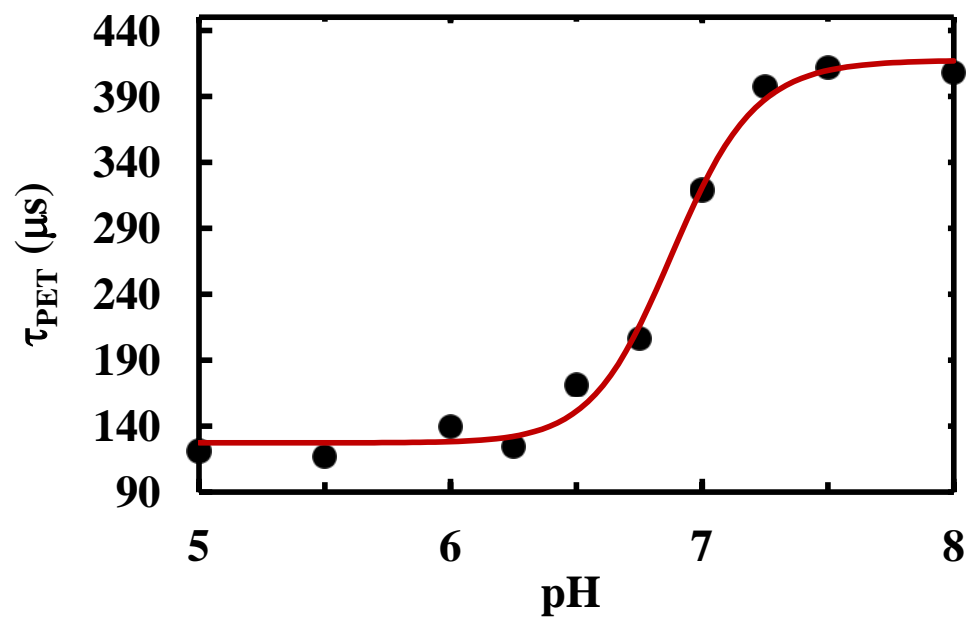


Figure 3. The plot of PET time constant to pH of M2TM with the lipid composition of POPC/POPG (4/1)

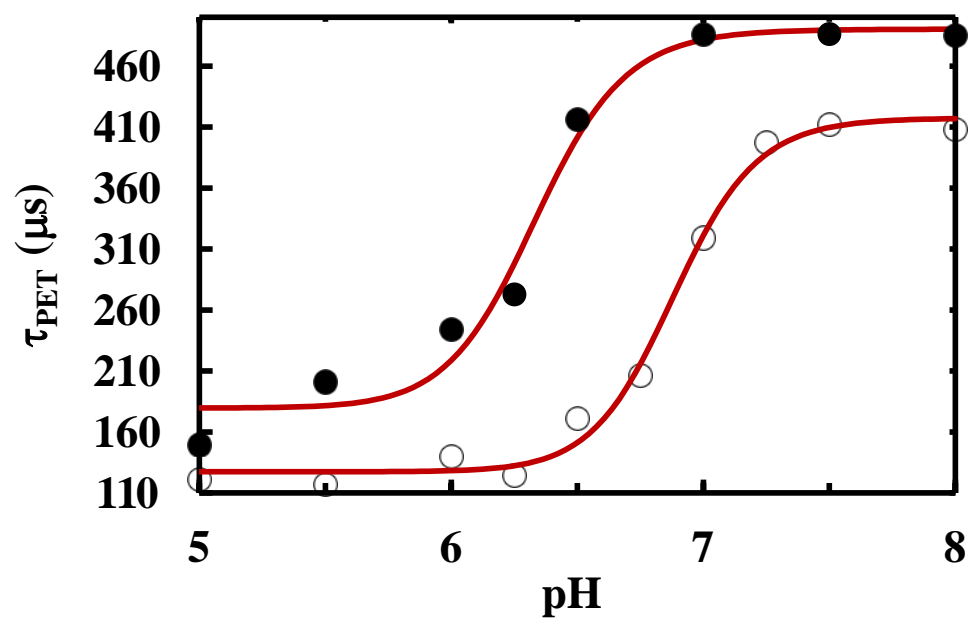


Figure 6.4. The plot of PET time constant to pH of M2TM. Empty circle denotes the experiments from the LUV made of POPC/POPG (4/1) and filled circle shows the experiments from LUV made of POPC/POPG/Cholesterol (4/1/2)

pH	5.00	5.50	6.00	6.25	6.50	7.00	7.50	8.00
τ_{PET}	149.5 μs	201.1 μs	244.0 μs	272.8 μs	416.0 μs	486.2 μs	486.3 μs	485.1 μs

Table 6.1. The PET time constants at different pH with the lipid composition of POPC/POPG/Cholesterol (4/1/2)

pH	5.00	5.50	6.00	6.25	6.50	6.75	7.00	7.25	7.50	8.00
	121.2	117.2	139.7	124.5	171.3	206.7	319.1	397.6	412.3	408.2
τ_{PET}	μs	μs	μs	μs	μs	μs	μs	μs	μs	μs

Table 6.2. The PET time constants at different pH with the lipid composition of POPC/POPG (4/1)

CHAPTER 7

Future Direction

In chapter 3, we show that the VIPT-jump experiment can be used to differentiate different folding mechanisms. In this study, we used the VIPT-jump experiment to differentiate the one state folder, BBL, from the two state folder, Trpzip-2c. An LD simulation was also used to support our experimental findings. In addition, by fitting kinetic traces with the LD simulations, we estimated the time needed to form a helical turn in the one state folder. For future directions, VIPT-jump experiment can be used to study the folding mechanism of intrinsically disordered peptides. Since these peptides do not have any secondary structure, it provides a unique opportunity to focus on the potential folding dynamics of the disordered state.

In chapter 4, we develop a model which can successfully provide fundamental folding information of the α -helical structure. It also shows its potential application in the folding dynamics of nonequilibrium helical reorganization. Some of these experiments incorporate a molecular photoswitch into the helical peptide which can create a sudden change in the thermally equilibrated distribution of the protein with the appropriate pulsed light source as the trigger. Both the thermodynamic data before and after the triggering process as well as the relaxation kinetics after the triggering process are fitted together to extract the fundamental folding rate constants of the peptide constrained by the triggering moiety.

In chapter 5, we combined an IR T -jump experiment with reverse micelles to slow down the heat dissipation from the nano water pool into the bulk nonpolar organic solvent. This thus made it possible to measure the folding dynamics from a slow folder, LysM, which used to be measured by stopped-flow experiments, by a T -jump experiment.

Ubiquitin was loaded into AOT reverse micelle to study the electrostatic interaction between the loaded protein and the negatively charged AOT surfactant layer, and the unusual formation of aggregation may lead to a future study of the mechanism on protein aggregation. Moreover, AOT reverse micelles of low w_0 are used as the model system to provide the environment of dehydration to induce the folding of the LEA peptide. However, the T -jump for the small size reverse micelle has to be improved before the further study of the folding dynamics in the reverse micelle of low w_0 .

In chapter 6, we showed that PET-FCS can be used to study the conformational dynamics of the M2 proton channel. The time constant of PET is attributed to the dynamics of the inter-helix motion, and shows a similar pH dependence as the titration curve of His37 in the M2 proton channel. The conformational dynamics should be included by future dynamics simulation studies to better model the proton conduction of the M2 proton channel. Understanding the dynamics of the M2 proton channel is key to unveiling the mechanism of the proton conduction; for example, why the channel has such high selectivity for protons and how the rate of the proton conduction is maintained. Further PET studies on the dynamics of the M2 proton channel with different types of PET pairs or different locations of PET pairs for global or local dynamics are indeed required.

References

1. Kendrew, J. C.; Bodo, G.; Dintzis, H. M.; Parrish, R. G.; Wyckoff, H.; Phillips, D. C., A Three-Dimensional Model of the Myoglobin Molecule Obtained by X-Ray Analysis. *Nature* **1958**, *181* (4610), 662-666.
2. Watson, J. D.; Crick, F. H. C., Molecular Structure of Nucleic Acids: A Structure for Deoxyribose Nucleic Acid. *Nature* **1953**, *171* (4356), 737-738.
3. Dill, K. A.; MacCallum, J. L., The Protein-Folding Problem, 50 Years On. *Science* **2012**, *338* (6110), 1042-1046.
4. Eaton, W. A., Searching for "downhill scenarios" in protein folding. *Proc. Natl. Acad. Sci. U.S.A.* **1999**, *96* (11), 5897-5899.
5. Garcia-Mira, M. M.; Sadqi, M.; Fischer, N.; Sanchez-Ruiz, J. M.; Munoz, V., Experimental Identification of Downhill Protein Folding. *Science* **2002**, *298* (5601), 2191-2195.
6. Shea, J.-E.; Onuchic, J. N.; Brooks, C. L., Probing the folding free energy landscape of the src-SH3 protein domain. *Proc. Natl. Acad. Sci. U.S.A.* **2002**, *99* (25), 16064-16068.
7. Cavalli, A.; Haberthür, U.; Paci, E.; Caflisch, A., Fast protein folding on downhill energy landscape. *Prot. Sci.* **2003**, *12* (8), 1801-1803.
8. Bunagan, M. R.; Yang, X.; Saven, J. G.; Gai, F., Ultrafast Folding of a Computationally Designed Trp-Cage Mutant: Trp2-Cage. *J. Phys. Chem. B* **2005**, *110* (8), 3759-3763.
9. Chiu, T. K.; Kubelka, J.; Herbst-Irmer, R.; Eaton, W. A.; Hofrichter, J.; Davies, D. R., High-resolution x-ray crystal structures of the villin headpiece subdomain,

- an ultrafast folding protein. *Proc. Natl. Acad. Sci. U.S.A.* **2005**, *102* (21), 7517-7522.
10. Ma, H.; Gruebele, M., Kinetics are probe-dependent during downhill folding of an engineered λ 6-85 protein. *Proc. Natl. Acad. Sci. U.S.A.* **2005**, *102* (7), 2283-2287.
 11. Xu, Y.; Purkayastha, P.; Gai, F., Nanosecond Folding Dynamics of a Three-Stranded β -Sheet. *J. Am. Chem. Soc.* **2006**, *128* (49), 15836-15842.
 12. Frauenfelder, H.; Sligar, S. G.; Wolynes, P. G., The Energy Landscapes and Motions of Proteins. *Science* **1991**, *254* (5038), 1598-1603.
 13. Bryngelson, J. D.; Onuchic, J. N.; Socci, N. D.; Wolynes, P. G., Funnels, pathways, and the energy landscape of protein folding: A synthesis. *Proteins* **1995**, *21* (3), 167-195.
 14. Guo, Z.; Brooks, C. L.; Boczko, E. M., Exploring the folding free energy surface of a three-helix bundle protein. *Proc. Natl. Acad. Sci. U.S.A.* **1997**, *94* (19), 10161-10166.
 15. Wolynes, P. G.; Onuchic, J. N.; Thirumalai, D., Navigating the Folding Routes. *Science* **1995**, *267* (5204), 1619-1620.
 16. Naganathan, A. N.; Doshi, U.; Fung, A.; Sadqi, M.; Munoz, V., Dynamics, Energetics, and Structure in Protein Folding. *Biochemistry* **2006**, *45* (28), 8466-8475.
 17. Li, P.; Oliva, F. Y.; Naganathan, A. N.; Munoz, V., Dynamics of one-state downhill protein folding. *Proc. Natl. Acad. Sci. U.S.A.* **2009**, *106* (1), 103-108.
 18. Dyer, R. B., Ultrafast and downhill protein folding. *Curr. Opin. Struct. Biol.* **2007**, *17* (1), 38-47.

19. Hagen, S. J., Exponential decay kinetics in “downhill” protein folding. *Proteins* **2003**, *50* (1), 1-4.
20. Ferguson, N.; Schartau, P. J.; Sharpe, T. D.; Sato, S.; Fersht, A. R., One-state Downhill versus Conventional Protein Folding. *J. Mol. Biol.* **2004**, *344* (2), 295-301.
21. Ferguson, N.; Sharpe, T. D.; Schartau, P. J.; Sato, S.; Allen, M. D.; Johnson, C. M.; Rutherford, T. J.; Fersht, A. R., Ultra-fast Barrier-limited Folding in the Peripheral Subunit-binding Domain Family. *J. Mol. Biol.* **2005**, *353* (2), 427-446.
22. Ferguson, N.; Sharpe, T. D.; Johnson, C. M.; Fersht, A. R., The Transition State for Folding of a Peripheral Subunit-binding Domain Contains Robust and Ionic-strength Dependent Characteristics. *J. Mol. Biol.* **2006**, *356* (5), 1237-1247.
23. Sadqi, M.; Fushman, D.; Munoz, V., Atom-by-atom analysis of global downhill protein folding. *Nature* **2006**, *442* (7100), 317-321.
24. Ferguson, N.; Sharpe, T. D.; Johnson, C. M.; Schartau, P. J.; Fersht, A. R., Structural Biology: Analysis of 'downhill' protein folding. *Nature* **2007**, *445* (7129), E14-E15.
25. Sadqi, M.; Fushman, D.; Munoz, V., Structural Biology: Analysis of 'downhill' protein folding; Analysis of protein-folding cooperativity (Reply). *Nature* **2007**, *445* (7129), E17-E18.
26. Naganathan, A. N.; Perez-Jimenez, R.; Sanchez-Ruiz, J. M.; Munoz, V., Robustness of Downhill Folding: Guidelines for the Analysis of Equilibrium Folding Experiments on Small Proteins. *Biochemistry* **2005**, *44* (20), 7435-7449.

27. Huang, C.; Klemke, J.; Getahun, Z.; DeGrado, W.; Gai, F., Temperature-dependent helix-coil transition of an alanine based peptide. *J. Am. Chem. Soc.* **2001**, *123* (38), 9235-9238.
28. Huang, C.-Y.; Getahun, Z.; Wang, T.; DeGrado, W. F.; Gai, F., Time-Resolved Infrared Study of the Helix-Coil Transition Using ¹³C-Labeled Helical Peptides. *J. Am. Chem. Soc.* **2001**, *123* (48), 12111-12112.
29. Qian, H.; Schellman, J. A., Helix-coil theories: a comparative study for finite length polypeptides. *J. Phys. Chem.* **1992**, *96* (10), 3987-3994.
30. Munoz, V.; Thompson, P. A.; Hofrichter, J.; Eaton, W. A., Folding dynamics and mechanism of β -hairpin formation. *Nature* **1997**, *390* (6656), 196-199.
31. Munoz, V.; Henry, E. R.; Hofrichter, J.; Eaton, W. A., A statistical mechanical model for α -hairpin kinetics. *Proc. Natl. Acad. Sci. U.S.A.* **1998**, *95* (11), 5872-5879.
32. Bertsch, R. A.; Vaidehi, N.; Chan, S. I.; Goddard, W. A., Kinetic steps for α -helix formation. *Proteins* **1998**, *33* (3), 343-357.
33. Ferrara, P.; Apostolakis, J.; Caflisch, A., Thermodynamics and kinetics of folding of two model peptides investigated by molecular dynamics simulations. *J. Phys. Chem. B* **2000**, *104* (20), 5000-5010.
34. Makarov, D. E.; Metiu, H., A model for the kinetics of protein folding: Kinetic Monte Carlo simulations and analytical results. *J. Chem. Phys.* **2002**, *116* (12), 5205-5216.
35. Nivon, L. G.; Shakhnovich, E. I., All-atom Monte Carlo Simulation of GCAA RNA Folding. *J. Mol. Biol.* **2004**, *344* (1), 29-45.

36. Carr, J. M.; Wales, D. J., Global optimization and folding pathways of selected alpha-helical proteins. *J. Chem. Phys.* **2005**, *123* (23), 234901-12.
37. Krieger, F.; Fierz, B.; Bieri, O.; Drewello, M.; Kiefhaber, T., Dynamics of unfolded polypeptide chains as model for the earliest steps in protein folding. *J. Mol. Biol.* **2003**, *332* (1), 265-274.
38. De Sancho, D.; Best, R. B., What Is the Time Scale for α -Helix Nucleation? *J. Am. Chem. Soc.* **2011**, *133* (17), 6809-6816.
39. Neumaier, S.; Reiner, A.; Buttner, M.; Fierz, B.; Kiefhaber, T., Testing the diffusing boundary model for the helix-coil transition in peptides. *Proc. Natl. Acad. Sci. U.S.A.* **2013**, *110* (32), 12905-12910.
40. Lin, C.-W.; Culik, R. M.; Gai, F., Using VIPT-Jump to Distinguish Between Different Folding Mechanisms: Application to BBL and a Trpzip. *J. Am. Chem. Soc.* **2013**, *135* (20), 7668-7673.
41. Dill, K. A.; Chan, H. S., From Levinthal to pathways to funnels. *Nat Struct Mol Biol* **1997**, *4* (1), 10-19.
42. Nakamura, H. K.; Sasai, M.; Takano, M., Squeezed exponential kinetics to describe a nonglassy downhill folding as observed in a lattice protein model. *Proteins* **2004**, *55* (1), 99-106.
43. Baumketner, A.; Shea, J. E., Free Energy Landscapes for Amyloidogenic Tetrapeptides Dimerization. *Biophys. J.* **2005**, *89* (3), 1493-1503.
44. Zuo, G.; Wang, J.; Wang, W., Folding with downhill behavior and low cooperativity of proteins. *Proteins* **2006**, *63* (1), 165-173.

45. Ghosh, K.; Ozkan, S. B.; Dill, K. A., The Ultimate Speed Limit to Protein Folding Is Conformational Searching. *J. Am. Chem. Soc.* **2007**, *129* (39), 11920-11927.
46. Mittal, J.; Best, R. B., Thermodynamics and kinetics of protein folding under confinement. *Proc. Natl. Acad. Sci. U.S.A.* **2008**, *105* (51), 20233-20238.
47. Sabelko, J.; Ervin, J.; Gruebele, M., Observation of strange kinetics in protein folding. *Proc. Natl. Acad. Sci. U.S.A.* **1999**, *96* (11), 6031-6036.
48. Knott, M.; Chan, H. S., Criteria for downhill protein folding: Calorimetry, chevron plot, kinetic relaxation, and single-molecule radius of gyration in chain models with subdued degrees of cooperativity. *Proteins* **2006**, *65* (2), 373-391.
49. Chung, H. S.; Tokmakoff, A., Temperature-dependent downhill unfolding of ubiquitin. I. Nanosecond-to-millisecond resolved nonlinear infrared spectroscopy. *Proteins* **2008**, *72* (1), 474-487.
50. Chung, H. S.; Tokmakoff, A., Temperature-dependent downhill unfolding of ubiquitin. II. Modeling the free energy surface. *Proteins* **2008**, *72* (1), 488-497.
51. Williams, S.; Causgrove, T. P.; Gilmanshin, R.; Fang, K. S.; Callender, R. H.; Woodruff, W. H.; Dyer, R. B., Fast Events in Protein Folding: Helix Melting and Formation in a Small Peptide. *Biochemistry* **1996**, *35* (3), 691-697.
52. Ballew, R. M.; Sabelko, J.; Gruebele, M., Direct observation of fast protein folding: the initial collapse of apomyoglobin. *Proc. Natl. Acad. Sci. U.S.A.* **1996**, *93* (12), 5759-5764.
53. Gilmanshin, R.; Williams, S.; Callender, R. H.; Woodruff, W. H.; Dyer, R. B., Fast events in protein folding: Relaxation dynamics of secondary and tertiary

- structure in native apomyoglobin. *Proc. Natl. Acad. Sci. U.S.A.* **1997**, *94* (8), 3709-3713.
54. Thompson, P. A.; Eaton, W. A.; Hofrichter, J., Laser Temperature Jump Study of the Helix \rightleftharpoons Coil Kinetics of an Alanine Peptide Interpreted with a 'Kinetic Zipper' Model. *Biochemistry* **1997**, *36* (30), 9200-9210.
55. Lednev, I. K.; Karnoup, A. S.; Sparrow, M. C.; Asher, S. A., α -Helix Peptide Folding and Unfolding Activation Barriers: A Nanosecond UV Resonance Raman Study. *J. Am. Chem. Soc.* **1999**, *121* (35), 8074-8086.
56. Leeson, D. T.; Gai, F.; Rodriguez, H. M.; Gregoret, L. M.; Dyer, R. B., Protein folding and unfolding on a complex energy landscape. *Proc. Natl. Acad. Sci. U.S.A.* **2000**, *97* (6), 2527-2532.
57. Huang, C.-Y.; Getahun, Z.; Zhu, Y.; Klemke, J. W.; DeGrado, W. F.; Gai, F., Helix formation via conformation diffusion search. *Proc. Natl. Acad. Sci. U.S.A.* **2002**, *99* (5), 2788-2793.
58. Wang, T.; Zhou, Z.; Bunagan, M. R.; Du, D.; Bai, Y.; Gai, F., Probing the folding intermediate of Rd-apocyt b₅₆₂ by protein engineering and infrared T-jump. *Prot. Sci.* **2007**, *16* (6), 1176-1183.
59. Liu, F.; Dumont, C.; Zhu, Y.; DeGrado, W. F.; Gai, F.; Gruebele, M., A one-dimensional free energy surface does not account for two-probe folding kinetics of protein α 3D. *J. Chem. Phys.* **2009**, *130* (6), 061101-5.
60. Xu, W.; Lai, Z.; Oliveira, R. J.; Leite, V. B. P.; Wang, J., Configuration-Dependent Diffusion Dynamics of Downhill and Two-State Protein Folding. *J. Phys. Chem. B* **2012**, *116* (17), 5152-5159.

61. Bai, Y.; Sosnick, T. R.; Leland, M.; Englander, S. W., Protein Folding Intermediates: Native-State Hydrogen Exchange. *Science* **1995**, *269* (5221), 192-197.
62. Pan, T.; Sosnick, T. R., Intermediates and kinetic traps in the folding of a large ribozyme revealed by circular dichroism and UV absorbance spectroscopies and catalytic activity. *Nat Struct Mol Biol* **1997**, *4* (11), 931-938.
63. Yang, W. Y.; Gruebele, M., Folding at the speed limit. *Nature* **2003**, *423* (6936), 193-197.
64. Yang, W. Y.; Gruebele, M., Folding λ -Repressor at Its Speed Limit. *Biophys. J.* **2004**, *87* (1), 596-608.
65. Chandler, D., *Modern Statistical Mechanics*. 1989.
66. Nitzan, A., *Chemical Dynamics in Condensed Phases*. 2006.
67. Munoz, V.; Sanchez-Ruiz, J. M., Exploring protein-folding ensembles: A variable-barrier model for the analysis of equilibrium unfolding experiments. *Proc. Natl. Acad. Sci. U.S.A.* **2004**, *101* (51), 17646-17651.
68. Prieto, L.; de Sancho, D.; Rey, A., Thermodynamics of Go-type models for protein folding. *J. Chem. Phys.* **2005**, *123* (15), 154903-8.
69. Bruscolini, P.; Pelizzola, A.; Zamparo, M., Downhill versus two-state protein folding in a statistical mechanical model. *J. Chem. Phys.* **2007**, *126* (21), 215103-8.
70. Cho, S. S.; Weinkam, P.; Wolynes, P. G., Origins of barriers and barrierless folding in BBL. *Proc. Natl. Acad. Sci. U.S.A.* **2008**, *105* (1), 118-123.

71. Pitera, J. W.; Swope, W. C.; Abraham, F. F., Observation of Noncooperative Folding Thermodynamics in Simulations of 1BBL. *Biophys. J.* **2008**, *94* (12), 4837-4846.
72. Zhang, J.; Li, W.; Wang, J.; Qin, M.; Wang, W., All-atom replica exchange molecular simulation of protein BBL. *Proteins* **2008**, *72* (3), 1038-1047.
73. Fan, J.; Duan, M.; Li, D.-W.; Wu, H.; Yang, H.; Han, L.; Huo, S., Observation of Two Families of Folding Pathways of BBL. *Biophys. J.* **2011**, *100* (10), 2457-2465.
74. Cochran, A. G.; Skelton, N. J.; Starovasnik, M. A., Tryptophan zippers: Stable, monomeric α -hairpins. *Proc. Natl. Acad. Sci. U.S.A.* **2001**, *98* (10), 5578-5583.
75. Du, D.; Zhu, Y.; Huang, C.-Y.; Gai, F., Understanding the key factors that control the rate of β -hairpin folding. *Proc. Natl. Acad. Sci. U.S.A.* **2004**, *101* (45), 15915-15920.
76. Huang, R.; Wu, L.; McElheny, D.; Bour, P.; Roy, A.; Keiderling, T. A., Cross-Strand Coupling and Site-Specific Unfolding Thermodynamics of a Trpzip α -Hairpin Peptide Using ^{13}C Isotopic Labeling and IR Spectroscopy. *J. Phys. Chem. B* **2009**, *113* (16), 5661-5674.
77. Shao, Q.; Wei, H.; Gao, Y. Q., Effects of Turn Stability and Side-Chain Hydrophobicity on the Folding of β -Structures. *J. Mol. Biol.* **2010**, *402* (3), 595-609.
78. Culik, R. M.; Jo, H.; DeGrado, W. F.; Gai, F., Using Thioamides To Site-Specifically Interrogate the Dynamics of Hydrogen Bond Formation in β -Sheet Folding. *J. Am. Chem. Soc.* **2012**, *134* (19), 8026-8029.

79. Barth, A.; Zscherp, C., What vibrations tell about proteins. *Q. Rev. Biophys.* **2002**, *35* (04), 369-430.
80. Fierz, B.; Reiner, A.; Kiefhaber, T., Local conformational dynamics in α -helices measured by fast triplet transfer. *Proc. Natl. Acad. Sci. U.S.A.* **2009**.
81. Serrano, A. L.; Tucker, M. J.; Gai, F., Direct Assessment of the α -Helix Nucleation Time. *J. Phys. Chem. B* **2011**, *115* (22), 7472-7478.
82. Serrano, A. L.; Waagele, M. M.; Gai, F., Spectroscopic studies of protein folding: Linear and nonlinear methods. *Prot. Sci.* **2012**, *21* (2), 157-170.
83. Roder, H., Stepwise helix formation and chain compaction during protein folding. *Proc. Natl. Acad. Sci. U.S.A.* **2004**, *101* (7), 1793-1794.
84. Clarke, D. T.; Doig, A. J.; Stapley, B. J.; Jones, G. R., The α -helix folds on the millisecond time scale. *Proc. Natl. Acad. Sci. U.S.A.* **1999**, *96* (13), 7232-7237.
85. Ascitutto, E. K.; Mikhonin, A. V.; Asher, S. A.; Madura, J. D., Computational and experimental determination of the α -helix unfolding reaction coordinate. *Biochemistry* **2008**, *47* (7), 2046-2050.
86. Ianoul, A.; Mikhonin, A.; Lednev, I. K.; Asher, S. A., UV resonance Raman study of the spatial dependence of α -helix unfolding. *J. Phys. Chem. A* **2002**, *106* (14), 3621-3624.
87. Lednev, I. K.; Karnoup, A. S.; Sparrow, M. C.; Asher, S. A., Transient UV raman spectroscopy finds no crossing barrier between the peptide α -helix and fully random coil conformation. *J. Am. Chem. Soc.* **2001**, *123* (10), 2388-2392.

88. Woutersen, S.; Hamm, P., Time-resolved two-dimensional vibrational spectroscopy of a short α -helix in water. *J. Chem. Phys.* **2001**, *115* (16), 7737-7743.
89. Backus, E. H. G.; Bloem, R.; Pfister, R.; Moretto, A.; Crisma, M.; Toniolo, C.; Hamm, P., Dynamical Transition in a Small Helical Peptide and Its Implication for Vibrational Energy Transport. *J. Phys. Chem. B* **2009**, *113* (40), 13405-13409.
90. Bredenbeck, J.; Helbing, J.; Kumita, J. R.; Woolley, G. A.; Hamm, P., α -Helix formation in a photoswitchable peptide tracked from picoseconds to microseconds by time-resolved IR spectroscopy. *Proc. Natl. Acad. Sci. U.S.A.* **2005**, *102* (7), 2379-2384.
91. Hamm, P.; Helbing, J.; Bredenbeck, J., Stretched versus compressed exponential kinetics in α -helix folding. *Chem. Phys.* **2006**, *323* (1), 54-65.
92. Abaskharon, Rachel M.; Gai, F., Meandering Down the Energy Landscape of Protein Folding: Are We There Yet? *Biophys. J.* **2016**, *110* (9), 1924-1932.
93. Zimm, B. H.; Bragg, J. K., Theory of the Phase Transition between Helix and Random Coil in Polypeptide Chains. *J. Chem. Phys.* **1959**, *31* (2), 526-535.
94. Lifson, S.; Roig, A., On the Theory of Helix—Coil Transition in Polypeptides. *J. Chem. Phys.* **1961**, *34* (6), 1963-1974.
95. Zwanzig, R., Simple model of protein folding kinetics. *Proc. Natl. Acad. Sci. U.S.A.* **1995**, *92* (21), 9801-9804.
96. Brooks, C. L., HelixCoil Kinetics: Folding Time Scales for Helical Peptides from a Sequential Kinetic Model. *J. Phys. Chem.* **1996**, *100* (7), 2546-2549.

97. Schwarz, G., On the kinetics of the helix-coil transition of polypeptides in solution. *J. Mol. Biol.* **1965**, *11* (1), 64-77.
98. Engel, J.; Schwarz, G., Cooperative Conformational Transitions of Linear Biopolymers. *Angew. Chem. Int. Ed.* **1970**, *9* (6), 389-400.
99. Thompson, P. A.; Muñoz, V.; Jas, G. S.; Henry, E. R.; Eaton, W. A.; Hofrichter, J., The Helix-Coil Kinetics of a Heteropeptide. *J. Phys. Chem. B* **2000**, *104* (2), 378-389.
100. Mohammed, O. F.; Jas, G. S.; Lin, M. M.; Zewail, A. H., Primary Peptide Folding Dynamics Observed with Ultrafast Temperature Jump. *Angew. Chem. Int. Ed.* **2009**, *48* (31), 5628-5632.
101. Tucker, M. J.; Abdo, M.; Courter, J. R.; Chen, J.; Brown, S. P.; Smith, A. B.; Hochstrasser, R. M., Nonequilibrium dynamics of helix reorganization observed by transient 2D IR spectroscopy. *Proc. Natl. Acad. Sci. U.S.A.* **2013**, *110* (43), 17314-17319.
102. Lin, M. M.; Shorokhov, D.; Zewail, A. H., Dominance of misfolded intermediates in the dynamics of α -helix folding. *Proc. Natl. Acad. Sci. U.S.A.* **2014**, *111* (40), 14424-14429.
103. Muñoz, V.; Eaton, W. A., A simple model for calculating the kinetics of protein folding from three-dimensional structures. *Proc. Natl. Acad. Sci. U.S.A.* **1999**, *96* (20), 11311-11316.
104. Luo, P.; Baldwin, R. L., Mechanism of Helix Induction by Trifluoroethanol: A Framework for Extrapolating the Helix-Forming Properties of Peptides from

- Trifluoroethanol/Water Mixtures Back to Water. *Biochemistry* **1997**, *36* (27), 8413-8421.
105. Scholtz, J. M.; Qian, H.; York, E. J.; Stewart, J. M.; Baldwin, R. L., Parameters of helix–coil transition theory for alanine-based peptides of varying chain lengths in water. *Biopolymers* **1991**, *31* (13), 1463-1470.
106. Miller, S. E.; Watkins, A. M.; Kallenbach, N. R.; Arora, P. S., Effects of side chains in helix nucleation differ from helix propagation. *Proc. Natl. Acad. Sci. U.S.A.* **2014**, *111* (18), 6636-6641.
107. Luo, P.; Baldwin, R. L., Interaction between water and polar groups of the helix backbone: An important determinant of helix propensities. *Proc. Natl. Acad. Sci. U.S.A.* **1999**, *96* (9), 4930-4935.
108. Muñoz, V.; Serrano, L., Development of the multiple sequence approximation within the AGADIR model of α -helix formation: Comparison with Zimm-Bragg and Lifson-Roig formalisms. *Biopolymers* **1997**, *41* (5), 495-509.
109. Davidon, W. C., Variable Metric Method for Minimization. *SIAM Journal on Optimization* **1991**, *1* (1), 1-17.
110. Dolan, E. D.; Lewis, R. M.; Torczon, V., On the Local Convergence of Pattern Search. *SIAM Journal on Optimization* **2003**, *14* (2), 567-583.
111. Piletic, I. R.; Moilanen, D. E.; Spry, D. B.; Levinger, N. E.; Fayer, M. D., Testing the Core/Shell Model of Nanoconfined Water in Reverse Micelles Using Linear and Nonlinear IR Spectroscopy. *J. Phys. Chem. A* **2006**, *110* (15), 4985-4999.
112. Fayer, M. D.; Levinger, N. E., Analysis of Water in Confined Geometries and at Interfaces. *Annu. Rev. Anal. Chem.* **2010**, *3* (1), 89-107.

113. Fenn, E. E.; Wong, D. B.; Giammanco, C. H.; Fayer, M. D., Dynamics of Water at the Interface in Reverse Micelles: Measurements of Spectral Diffusion with Two-Dimensional Infrared Vibrational Echoes. *J. Phys. Chem. B* **2011**, *115* (40), 11658-11670.
114. Komives, C. F.; Osborne, D. E.; Russell, A. J., Characterization of a nonionic surfactant reversed micellar system for enzyme catalysis. *J. Phys. Chem.* **1994**, *98* (1), 369-376.
115. Wand, A. J.; Ehrhardt, M. R.; Flynn, P. F., High-resolution NMR of encapsulated proteins dissolved in low-viscosity fluids. *Proc. Natl. Acad. Sci. U.S.A.* **1998**, *95* (26), 15299-15302.
116. Babu, C. R.; Flynn, P. F.; Wand, A. J., Validation of Protein Structure from Preparations of Encapsulated Proteins Dissolved in Low Viscosity Fluids. *J. Am. Chem. Soc.* **2001**, *123* (11), 2691-2692.
117. Peterson, R. W.; Anbalagan, K.; Tommos, C.; Wand, A. J., Forced Folding and Structural Analysis of Metastable Proteins. *J. Am. Chem. Soc.* **2004**, *126* (31), 9498-9499.
118. Mukherjee, S.; Chowdhury, P.; DeGrado, W. F.; Gai, F., Site-Specific Hydration Status of an Amphipathic Peptide in AOT Reverse Micelles. *Langmuir* **2007**, *23* (22), 11174-11179.
119. Glasscock, J. M.; Zhu, Y.; Chowdhury, P.; Tang, J.; Gai, F., Using an Amino Acid Fluorescence Resonance Energy Transfer Pair To Probe Protein Unfolding: Application to the Villin Headpiece Subdomain and the LysM Domain. *Biochemistry* **2008**, *47* (42), 11070-11076.

120. Getahun, Z.; Huang, C.-Y.; Wang, T.; De León, B.; DeGrado, W. F.; Gai, F., Using Nitrile-Derivatized Amino Acids as Infrared Probes of Local Environment. *J. Am. Chem. Soc.* **2003**, *125* (2), 405-411.
121. Jo, H.; Culik, R. M.; Korendovych, I. V.; DeGrado, W. F.; Gai, F., Selective Incorporation of Nitrile-Based Infrared Probes into Proteins via Cysteine Alkylation. *Biochemistry* **2010**, *49* (49), 10354-10356.
122. Urbanek, D. C.; Vorobyev, D. Y.; Serrano, A. L.; Gai, F.; Hochstrasser, R. M., The Two Dimensional Vibrational Echo of a Nitrile Probe of the Villin HP35 Protein. *J Phys Chem Lett* **2010**, *1* (23), 3311-3315.
123. Waegele, M. M.; Gai, F., Computational Modeling of the Nitrile Stretching Vibration of 5-Cyanoindole in Water. *J Phys Chem Lett* **2010**, *1* (4), 781-786.
124. Mukherjee, D.; Gai, F., Exciton circular dichroism couplet arising from nitrile-derivatized aromatic residues as a structural probe of proteins. *Anal. Biochem.* **2016**, *507*, 74-78.
125. Waegele, M. M.; Culik, R. M.; Gai, F., Site-Specific Spectroscopic Reporters of the Local Electric Field, Hydration, Structure, and Dynamics of Biomolecules. *J Phys Chem Lett* **2011**, *2* (20), 2598-2609.
126. Qun-Fang, L.; Rui-Sen, L.; Dan-Yan, N.; Yu-Chun, H., Thermal Conductivities of Some Organic Solvents and Their Binary Mixtures. *Journal of Chemical & Engineering Data* **1997**, *42* (5), 971-974.
127. Ding, B.; Hilaire, M. R.; Gai, F., Infrared and Fluorescence Assessment of Protein Dynamics: From Folding to Function. *J. Phys. Chem. B* **2016**, *120* (23), 5103-5113.

128. Pinto, L. H.; Lamb, R. A., The M2 Proton Channels of Influenza A and B Viruses. *J. Biol. Chem.* **2006**, *281* (14), 8997-9000.
129. Shimbo, K.; Brassard, D. L.; Lamb, R. A.; Pinto, L. H., Ion selectivity and activation of the M2 ion channel of influenza virus. *Biophys. J.* **1996**, *70* (3), 1335-1346.
130. Hay, A. J.; Wolstenholme, A. J.; Skehel, J. J.; Smith, M. H., *EMBO J.* **1985**, *4*, 3021.
131. Schnell, J. R.; Chou, J. J., Structure and mechanism of the M2 proton channel of influenza A virus. *Nature* **2008**, *451* (7178), 591-595.
132. Pielak, R. M.; Schnell, J. R.; Chou, J. J., Mechanism of drug inhibition and drug resistance of influenza A M2 channel. *Proc. Natl. Acad. Sci. U.S.A.* **2009**, *106* (18), 7379-7384.
133. Cady, S. D.; Schmidt-Rohr, K.; Wang, J.; Soto, C. S.; DeGrado, W. F.; Hong, M., Structure of the amantadine binding site of influenza M2 proton channels in lipid bilayers. *Nature* **2010**, *463* (7281), 689-692.
134. Balannik, V.; Carnevale, V.; Fiorin, G.; Levine, B. G.; Lamb, R. A.; Klein, M. L.; DeGrado, W. F.; Pinto, L. H., Functional Studies and Modeling of Pore-Lining Residue Mutants of the Influenza A Virus M2 Ion Channel. *Biochemistry* **2010**, *49* (4), 696-708.
135. Wu, Y.; Canturk, B.; Jo, H.; Ma, C.; Gianti, E.; Klein, M. L.; Pinto, L. H.; Lamb, R. A.; Fiorin, G.; Wang, J.; DeGrado, W. F., Flipping in the Pore: Discovery of Dual Inhibitors That Bind in Different Orientations to the Wild-Type versus the

- Amantadine-Resistant S31N Mutant of the Influenza A Virus M2 Proton Channel. *J. Am. Chem. Soc.* **2014**, *136* (52), 17987-17995.
136. Pielak, R. M.; Chou, J. J., Influenza M2 proton channels. *Biochimica et Biophysica Acta (BBA) - Biomembranes* **2011**, *1808* (2), 522-529.
137. Sansom, M. S. P.; Kerr, I. D.; Smith, G. R.; Son, H. S., The Influenza A Virus M2 Channel: A Molecular Modeling and Simulation Study. *Virology* **1997**, *233* (1), 163-173.
138. Smondyrev, A. M.; Voth, G. A., Molecular Dynamics Simulation of Proton Transport through the Influenza A Virus M2 Channel. *Biophys. J.* **2002**, *83* (4), 1987-1996.
139. Kass, I.; Arkin, I. T., How pH Opens a H⁺ Channel: The Gating Mechanism of Influenza A M2. *Structure* **2005**, *13* (12), 1789-1798.
140. Pinto, L. H.; Dieckmann, G. R.; Gandhi, C. S.; Papworth, C. G.; Braman, J.; Shaughnessy, M. A.; Lear, J. D.; Lamb, R. A.; DeGrado, W. F., A functionally defined model for the M2 proton channel of influenza A virus suggests a mechanism for its ionselectivity. *Proc. Natl. Acad. Sci. U.S.A.* **1997**, *94* (21), 11301-11306.
141. Gandhi, C. S.; Shuck, K.; Lear, J. D.; Dieckmann, G. R.; DeGrado, W. F.; Lamb, R. A.; Pinto, L. H., Cu(II) Inhibition of the Proton Translocation Machinery of the Influenza A Virus M2 Protein. *J. Biol. Chem.* **1999**, *274* (9), 5474-5482.
142. Schweighofer, K. J.; Pohorille, A., Computer Simulation of Ion Channel Gating: The M2 Channel of Influenza A Virus in a Lipid Bilayer. *Biophys. J.* **2000**, *78* (1), 150-163.

143. Fiorin, G.; Carnevale, V.; DeGrado, W. F., The Flu's Proton Escort. *Science* **2010**, *330* (6003), 456-458.
144. Hu, F.; Luo, W.; Hong, M., Mechanisms of Proton Conduction and Gating in Influenza M2 Proton Channels from Solid-State NMR. *Science* **2010**, *330* (6003), 505-508.
145. Hu, F.; Schmidt-Rohr, K.; Hong, M., NMR Detection of pH-Dependent Histidine–Water Proton Exchange Reveals the Conduction Mechanism of a Transmembrane Proton Channel. *J. Am. Chem. Soc.* **2012**, *134* (8), 3703-3713.
146. Williams, Jonathan K.; Zhang, Y.; Schmidt-Rohr, K.; Hong, M., pH-Dependent Conformation, Dynamics, and Aromatic Interaction of the Gating Tryptophan Residue of the Influenza M2 Proton Channel from Solid-State NMR. *Biophys. J.* **2013**, *104* (8), 1698-1708.
147. DiFrancesco, M. L.; Hansen, U.-P.; Thiel, G.; Moroni, A.; Schroeder, I., Effect of Cytosolic pH on Inward Currents Reveals Structural Characteristics of the Proton Transport Cycle in the Influenza A Protein M2 in Cell-Free Membrane Patches of *Xenopus* oocytes. *PLoS One* **2014**, *9* (9), e107406.
148. Zhou, H.-X., A Theory for the Proton Transport of the Influenza Virus M2 Protein: Extensive Test against Conductance Data. *Biophys. J.* **2011**, *100* (4), 912-921.
149. Markiewicz, B. N.; Lemmin, T.; Zhang, W.; Ahmed, I. A.; Jo, H.; Fiorin, G.; Troxler, T.; DeGrado, W. F.; Gai, F., Infrared and fluorescence assessment of the hydration status of the tryptophan gate in the influenza A M2 proton channel. *PCCP* **2016**, *18* (41), 28939-28950.

150. Marmé, N.; Knemeyer, J. P.; Sauer, M.; Wolfrum, J., *Bioconjugate Chem.* **2003**, *14*, 1133.
151. Doose, S.; Neuweiler, H.; Sauer, M., A Close Look at Fluorescence Quenching of Organic Dyes by Tryptophan. *ChemPhysChem* **2005**, *6* (11), 2277-2285.
152. Neuweiler, H.; Johnson, C. M.; Fersht, A. R., Direct observation of ultrafast folding and denatured state dynamics in single protein molecules. *Proc. Natl. Acad. Sci. U.S.A.* **2009**, *106* (44), 18569-18574.
153. Doose, S.; Neuweiler, H.; Sauer, M., Fluorescence Quenching by Photoinduced Electron Transfer: A Reporter for Conformational Dynamics of Macromolecules. *ChemPhysChem* **2009**, *10* (9-10), 1389-1398.
154. Lum, J. K.; Neuweiler, H.; Fersht, A. R., Long-Range Modulation of Chain Motions within the Intrinsically Disordered Transactivation Domain of Tumor Suppressor p53. *J. Am. Chem. Soc.* **2012**, *134* (3), 1617-1622.
155. Rogers, J. M. G.; Polishchuk, A. L.; Guo, L.; Wang, J.; DeGrado, W. F.; Gai, F., Photoinduced Electron Transfer and Fluorophore Motion as a Probe of the Conformational Dynamics of Membrane Proteins: Application to the Influenza A M2 Proton Channel. *Langmuir* **2011**, *27* (7), 3815-3821.
156. Cristian, L.; Lear, J. D.; DeGrado, W. F., Use of thiol-disulfide equilibria to measure the energetics of assembly of transmembrane helices in phospholipid bilayers. *Proc. Natl. Acad. Sci. U.S.A.* **2003**, *100* (25), 14772-14777.
157. Stouffer, A. L.; Nanda, V.; Lear, J. D.; DeGrado, W. F., Sequence Determinants of a Transmembrane Proton Channel: An Inverse Relationship between Stability and Function. *J. Mol. Biol.* **2005**, *347* (1), 169-179.

158. Salom, D.; Hill, B. R.; Lear, J. D.; DeGrado, W. F., pH-Dependent Tetramerization and Amantadine Binding of the Transmembrane Helix of M2 from the Influenza A Virus. *Biochemistry* **2000**, *39* (46), 14160-14170.
159. Ma, C.; Polishchuk, A. L.; Ohigashi, Y.; Stouffer, A. L.; Schön, A.; Magavern, E.; Jing, X.; Lear, J. D.; Freire, E.; Lamb, R. A.; DeGrado, W. F.; Pinto, L. H., Identification of the functional core of the influenza A virus A/M2 proton-selective ion channel. *Proc. Natl. Acad. Sci. U.S.A.* **2009**, *106* (30), 12283-12288.
160. Guo, L.; Chowdhury, P.; Glasscock, J. M.; Gai, F., Denaturant-induced Expansion and Compaction of a Multi-domain Protein: IgG. *J. Mol. Biol.* **2008**, *384* (5), 1029-1036.